The Astrophysical Journal, 979:211 (18pp), 2025 February 1 https://doi.org/10.3847/1538-4357/ad9f2f

Constraining Solar Wind Transport Model Parameters Using Bayesian Analysis

Mark A. Bishop[1,2], Sean Oughton[2], Tulasi N. Parashar[1], and Yvette C. Perrott[1]
[1] School of Chemical and Physical Sciences, Victoria University of Wellington, Wellington 6012, New Zealand; mark.bishop@vuw.ac.nz
[2] Department of Mathematics, University of Waikato, Hamilton 3240, New Zealand
Received 2024 September 3; revised 2024 November 18; accepted 2024 December 9; published 2025 January 28

Abstract

We apply nested-sampling Bayesian analysis to a model for the transport of magnetohydrodynamic-scale solar wind fluctuations. The dual objectives are to obtain improved constraints on parameters present in the turbulence transport model (TTM) and to support quantitative comparisons of the quality of distinct versions of the transport model. The TTMs analyzed are essentially the 1D steady-state ones presented in Breech et al. that describe the radial evolution of the energy, correlation length, and normalized cross helicity of the fluctuations, together with the proton temperature, in prescribed background solar wind fields. Modeled effects present in the TTM include nonlinear turbulence interactions, shear driving, and energy injection associated with pickup-ions. Each of these modeled effects involves adjustable parameters that we seek to constrain using Bayesian analysis. We find that, given the TTMs and observational data sets analyzed, the most appropriate TTM to recommend corresponds to 2D fluctuations and has von Kármán–Howarth parameters of $\alpha \approx 0.16$ and $\beta \approx 0.10$, along with reasonably standard values for the other adjustable parameters. The analysis also indicates that it is advantageous to include pickup ion effects in the lengthscale evolution equation by assuming $Z^{2\,\beta/\alpha}\lambda$ is locally conserved. Such Bayesian analysis is readily extended to more sophisticated solar wind models, space weather models, and might lead to improved predictions of, for example, solar flare and coronal mass ejection interactions with the Earth.

Unified Astronomy Thesaurus concepts: Interplanetary turbulence (830); Solar wind (1534); Magnetohydrodynamics (1964)

1. Introduction

The evolution of magnetohydrodynamic (MHD) scale fluctuations in the solar wind is a topic of long-standing interest, with relevance to various aspects of space physics including space weather (R. Schwenn 2006), scattering of cosmic rays (C. Pei et al. 2010; N. E. Engelbrecht et al. 2022), and their roles in connection with the global evolution of the heliospheric fields (e.g., B. van der Holst et al. 2014; N. V. Pogorelov et al. 2024). Under various assumptions and approximations, this evolution has been investigated observationally, theoretically, and numerically (for recent reviews, see R. Bruno & V. Carbone 2013; S. Oughton & N. E. Engelbrecht 2021; F. Fraternale et al. 2022; C. W. Smith & B. J. Vasquez 2024). Early models were based on the WKB approximation and treated the fluctuations as MHD waves (E. N. Parker 1965). Transport models that accounted for turbulence fluctuations (as well as waves) were presented in the 1980s (C.-Y. Tu et al. 1984; C. Tu 1987; M. Velli et al. 1989; Y. Zhou & W. H. Matthaeus 1990; C.-Y. Tu & E. Marsch 1995). Extensions of these turbulence transport models (TTMs) support time-dependence, three-dimensionality, and driving by stream shear and pickup ion (PI) induced waves, and interactions in the heliosheath and local interstellar medium.

Many of these TTMs belong to the "energy-containing" class (W. H. Matthaeus et al. 1994, 1996b; G. P. Zank et al. 1996), meaning that they evolve *bulk* characteristics of the turbulence (such as its energy and correlation length), rather than tracking, for example, energy spectra. These typically involve modeling of the nonlinear terms associated with turbulence and also of driving processes, usually with adjustable parameters being features of the modeling. The question of how to best determine these adjustable parameters is a primary focus of this work.

Beyond 1 au or so, agreement between observations and TTM simulation results is, typically, encouraging (e.g., C. W. Smith et al. 2001; B. Breech et al. 2008; L. Adhikari et al. 2021; F. Fraternale et al. 2022; C. W. Smith & B. J. Vasquez 2024). However, the modeling parameters used in such studies have usually been estimated in rather ad hoc fashion with few systematic efforts made to find optimal or best-fit values. For example, two common approaches are (i) generating "best-fitting" values based on guess-and-check, and then by-eye validation against solar wind observations, and (ii) displaying several solutions corresponding to different values of the adjustable parameters (e.g., G. P. Zank et al. 1996; W. H. Matthaeus et al. 1999; C. W. Smith et al. 2001; B. Breech et al. 2008; S. Oughton et al. 2011; A. V. Usmanov et al. 2018; L. Adhikari et al. 2015, 2021). Although these approaches have had considerable success, it would of course be preferable to employ a systematic method for constraining any adjustable parameters present in the TTMs. Ideally, this constraining method would be based on both the TTM and the solar wind data, and also provide a statistically rigorous way of comparing TTMs to one another. Bayesian analysis methodologies, which determine (posterior) probability distributions for model parameters from imposed prior distributions and data, can address both of these aspects. Our objective herein is to show how Bayesian analysis can be used to constrain and compare solar wind transport models.

The most sophisticated energy-containing TTMs are time dependent, 3D, and can provide (numerical) solutions throughout the heliosphere and, in some cases, into the local interstellar medium (e.g., A. V. Usmanov et al. 2011, 2014, 2016;

T. Wiengarten et al. 2015, 2016; D. Shiota et al. 2017; J. Kleimann et al. 2023). See F. Fraternale et al. (2022) for a review. In many applications, however, the simplified situation of a steady-state, spherically symmetric, and 1D (radial) heliosphere is of relevance (e.g., W. H. Matthaeus et al. 1994; W. H. Matthaeus et al. 1996b, 1999; G. P. Zank et al. 1996; C. W. Smith et al. 2001; B. Breech et al. 2008; S. Oughton et al. 2011; L. Adhikari et al. 2015, 2017a, 2021, 2023). Naturally, this affords considerable numerical advantages and even allows determination of some analytic solutions (W. H. Matthaeus et al. 1996b; G. P. Zank et al. 1996; S. Oughton & M. A. Bishop 2025, in preparation). Hereafter, we focus on this simplified steady 1D situation, applying Bayesian analysis to essentially the TTMs presented in B. Breech et al. (2008). Use of a simpler TTM facilitates a clean presentation of the approach, which to the best of our knowledge represents the first time Bayesian analysis has been used with a solar wind TTM.

Bayesian methodologies have been used extensively in the fields of astronomy and cosmology (see R. Trotta 2008, for a review). Well-known examples include constraining the Hubble constant on Type Ia supernovae data (S. Perlmutter et al. 1995; T. M. C. Abbott et al. 2019), and constraining the other cosmological constants based on cosmic microwave background observations (G. Jungman et al. 1996; Planck Collaboration et al. 2020). On the astronomy side, applications have included various profile fittings (K. Javid et al. 2019; Y. C. Perrott et al. 2019) and determination of many different astrophysical parameters (see, e.g., D. Parkinson & A. R. Liddle 2013; S. Sharma 2017, and references therein).

These techniques have also been used in other assorted disciplines. See G. Ashton et al. (2022) for a review with a focus on the nested-sampling method that we employ herein (see Appendix C) and A. M. Ellison (2004), U. von Toussaint (2011), Y. Huang et al. (2019), and R. van de Schoot et al. (2021) for more general Bayesian inference application reviews.

As a consequence of this extensive use of Bayesian analysis, many software packages have been developed, including ones designed explicitly for applications in astronomy and astrophysics (F. Feroz et al. 2009; B. J. Brewer et al. 2010; E. Corsaro & J. De Ridder 2014; J. S. Speagle 2020; K. Barbary 2021; J. Buchner 2021; D. Kester & M. Mueller 2021) and cosmology (A. Hojjati et al. 2011; D. Parkinson et al. 2011; W. J. Handley et al. 2015). In performing our analysis, we will make use of some of this public domain software.

The structure of the paper is as follows. In Section 2, we summarize the TTMs and observational data sets to which we apply Bayesian analysis. The Bayesian analysis technique is outlined in Section 3 with the results of the analyses presented in Section 4. Section 5 contains discussion of the results, followed by a conclusion section. Two appendices close the paper, presenting further details regarding the TTMs (Appendix A) and Bayesian methodologies (Appendix C).

2. The Turbulence Transport Models

2.1. Model Equations

We employ a previously developed (B. Breech et al. 2008) TTM that assumes a 1D (radial r) steady-state large-scale solar wind with uniform flow speed $U\hat{\boldsymbol{r}}$, density $\rho \propto 1/r^2$, and Alfvén speed $\boldsymbol{V}_A(r)$. Three quantities characterizing the incompressible turbulence fluctuations are followed—energy Z^2, correlation length λ, and normalized cross helicity σ_c—plus the proton temperature T. We solve the TTM in the super-Alfvénic flow region, neglecting terms of order V_A/U to obtain (see Appendix A)

$$U\frac{dZ^2}{dr} = -\frac{UZ^2}{r}[1 + \sigma_D M_Z - C_{\rm sh}] + \dot{E}_{\rm PI} - \alpha f^+(\sigma_c)\frac{Z^3}{\lambda}, \tag{1}$$

$$U\frac{d\lambda}{dr} = \frac{\lambda\sigma_D M_\lambda U}{r} + \beta f^+(\sigma_c)Z - \frac{\beta}{\alpha}\frac{\lambda}{Z^2}\dot{E}_{\rm PI}\,, \tag{2}$$

$$U\frac{d\sigma_c}{dr} = \alpha f'(\sigma_c)\frac{Z}{\lambda} - \left[\frac{U}{r}(C_{\rm sh} - \sigma_D M_Z) + \frac{\dot{E}_{\rm PI}}{Z^2}\right]\sigma_c, \tag{3}$$

$$U\frac{dT}{dr} = -\frac{4}{3}\frac{TU}{r} + \frac{\alpha}{3}\frac{m_p}{k_{\rm B}}f^+(\sigma_c)\frac{Z^3}{\lambda}, \tag{4}$$

where $f^\pm(\sigma_c) = \sqrt{1-\sigma_c^2}[\sqrt{1+\sigma_c} \pm \sqrt{1-\sigma_c}]/2$, $f'(\sigma_c) = \sigma_c f^+(\sigma_c) - f^-(\sigma_c)$, m_p is the proton mass, $k_{\rm B}$ is Boltzmann's constant, and the other quantities are discussed below. Terms in the equations represent physics associated with advection by the mean wind, large-scale gradient "mixing" effects, and modeling of energy dissipation and driving (B. Breech et al. 2008). The TTM is appropriate for any helio-colatitude θ, although here we restrict our analysis to ecliptic cases, i.e., $\theta = \pi/2$.

One sees that the TTM depends on the so-called "mixing operators," M_Z and M_λ, that take different forms depending upon the underlying symmetry of the fluctuations. We suppose that the fluctuations have one of two distinct symmetries: either 3D isotropic or 2D isotropic, where the latter means the fluctuation amplitudes are restricted to be perpendicular to the mean (Parker spiral) magnetic field and to be isotropically distributed in those 2D planes. For brevity, we refer to these two cases as the 3D and 2D models. Under the stated assumptions, one obtains (W. H. Matthaeus et al. 1994, 1996b; G. P. Zank et al. 1996; B. Breech et al. 2008)

$$\text{3D model:}\quad M_Z = \frac{1}{3},\ M_\lambda = \frac{1}{3}, \tag{5}$$

$$\text{2D model:}\quad M_Z = \cos^2\psi,\ M_\lambda = \sin^2\psi, \tag{6}$$

where $\psi(r)$ is the angle between the mean interplanetary magnetic field, taken to be a E. N. Parker (1958) spiral, and the radial direction. For definiteness, we employ the Parker spiral associated with an Alfvén radius of 10 solar radii, and a solar rotation rate of 2.9×10^{-6} rad s^{-1}.

Also present in the TTM are five adjustable parameters: α, β, $C_{\rm sh}$, f_D, σ_D. It is these, along with the four inner boundary conditions (BCs), that we will use Bayesian analysis to constrain. Physically, the parameters relate to von Kármán–Howarth (vKH) style modeling of the turbulent energy cascade (α and β), modeling of stream shear driving ($C_{\rm sh}$) and pickup ion driving (f_D, see Equation (8)), and a closure for the energy difference (σ_D). In the next subsection, we discuss several points concerning these parameters and the application of Bayesian analysis to them. For further discussion of the physics associated with the modeling and adjustable parameters, see, for example, B. Breech et al. (2008).

To provide a clean presentation of the Bayesian analysis approach for determining the TTM parameters, we have chosen

to use relatively simple TTMs. (Application to more complete and/or sophisticated TTMs, as referenced in Section 1, is left for future work.) For example, we employ a uniform wind speed of $U = 400$ km s^{-1} and neglect features such as transport terms of order V_A/U and the decrease of $U(r)$ with distance (C. Wang & J. Richardson 2003; P. A. Isenberg et al. 2010; G. P. Zank et al. 2018; H. A. Elliott et al. 2019). Furthermore, the modeling of energy injection, associated with either velocity shear (at constant correlation length) or pickup ion instabilities, is rather simple, with more developed modeling approaches available (e.g., P. A. Isenberg 2005; G. P. Zank et al. 2012; T. Wiengarten et al. 2015). Such extensions can be readily incorporated. We remark that the modeling approaches for the shear and pickup ion driving differ; see B. Breech et al. (2008) for more details.

We have also made the simplifying assumption that all of the cascaded turbulence energy is used to heat solar wind protons. Of course, this is unlikely to be realistic, with studies indicating that about 40% of the turbulence energy heats solar wind electrons instead (B. Breech et al. 2009; S. R. Cranmer et al. 2009; G. G. Howes 2011). Relaxation of this "proton only" heating assumption is considered in Appendix B.

2.2. Estimation of Adjustable Parameters

As noted in the Introduction, previous studies have often estimated adjustable parameters in a TTM in somewhat ad hoc or nonsystematic ways. Here, we give brief descriptions of some of these methods and indicate how one may instead apply Bayesian analysis.

Let us start with the vKH parameters α and β. Values for these have sometimes been chosen on the basis of results from homogeneous decaying MHD turbulence simulations (M. Hossain et al. 1995; M. Linkmann et al. 2017; R. Bandyopadhyay et al. 2018, 2019). In other cases, α has been set by extending the equivalent experimentally determined quantity for homogeneous decaying Navier–Stokes turbulence (K. R. Sreenivasan 1998) to MHD (A. V. Usmanov et al. 2014; D. Wrench et al. 2024). In either situation, a value for β can be assigned by imposing one of the conservation laws from the family applicable in homogeneous turbulence cases, $Z^{2\beta/\alpha}\lambda =$ const, with the ratios $2\beta/\alpha = 1$ or 2 of particular physical significance (M. Hossain et al. 1995; W. H. Matthaeus et al. 1996b; G. P. Zank et al. 1996, 2012; M. Wan et al. 2012). These are of course physically well-motivated approaches. However, they are unlikely to provide values that can provide optimal fits to data, motivating our application of Bayesian analysis to determine posterior probability distributions for these parameters.

Consider now the σ_D parameter appearing in Equations (1)–(3). This arises because, in place of a dynamical equation for the energy difference $D = E^v - E^b$ (aka residual energy), we employ the approximation that the normalized energy difference, $\sigma_D = D/Z^2 \equiv (E^v - E^b)/(E^v + E^b)$, is a constant ($E^v$, E^b are the fluctuation kinetic and magnetic energies). On the basis of solar wind observations (e.g., S. Perri & A. Balogh 2010), the choice $\sigma_D \approx -1/3$ has frequently been used in TTMs (e.g., W. H. Matthaeus et al. 1996b; G. P. Zank et al. 1996; C. W. Smith et al. 2001; B. Breech et al. 2008; N. Yokoi et al. 2008; S. Oughton et al. 2011). In Section 4.2, we will employ Bayesian analysis to investigate the appropriateness of using $\sigma_D =$ const. Moreover, even though we treat it as a constant, we shall see in Section 3 that it is advantageous to nonetheless include σ_D in the Bayesian analysis likelihood calculations (see Section 3). Implementation wise, this is equivalent to adding the evolution equation

$$\frac{d\sigma_D}{dr} = 0 \tag{7}$$

to the system Equations (1)–(4); clearly, this leads to σ_D being equal to its inner boundary value.

Table 1
Some TTM Parameters Common to the 3D and 2D Isotropic Models

Quantity	Value
U	400 km s^{-1}
σ_D	$-1/3$
$C_{\rm sh}$	1.5
f_D	0.25
$L_{\rm cav}$	8 au
$n_{\rm H}^{\infty}$	0.1 cm^{-3}
$n_{\rm SW}^{1\,\rm au}$	5 cm^{-3}
$\tau_{\rm ion}^{1\,\rm au}$	1×10^6 s

Note. Parameters in the lower section are associated with forcing and are as used in B. Breech et al. (2008). We refer to these values as the "nominal" estimates.

Estimates for $C_{\rm sh}$, the constant determining the strength of the driving due to large-scale velocity shear (L. F. Burlaga 1974; E. J. Smith & J. H. Wolfe 1976; M. Neugebauer et al. 1995), have primarily been set using simple theoretical models of shear evaluated using typical observational values (e.g., G. P. Zank et al. 1996; W. H. Matthaeus et al. 1999; C. W. Smith et al. 2001; B. Breech et al. 2008). There is thus some similarity with the approach used in determining σ_D. We follow B. Breech et al. (2008) in modeling the shear interaction between faster and slower streams of the solar wind. In particular, the shear driving is assumed to occur at the correlation length scale, and thus, there is no explicit shear driving term in the λ Equation (2) (B. Breech et al. 2005).

The final adjustable parameter to consider, f_D, controls the overall strength of the energy injection associated with waves generated by the scattering of pickup ions. Here, we model the process using (L. L. Williams & G. P. Zank 1994; G. P. Zank et al. 1996; W. H. Matthaeus et al. 1999; C. W. Smith et al. 2001; B. Breech et al. 2008)[3]

$$\frac{\dot{E}_{\rm PI}}{U} = f_D \frac{V_A n_{\rm H}^{\infty}}{n_{\rm SW}^{1\,\rm au}\,\tau_{\rm ion}^{1\,\rm au}} e^{-L_{\rm cav}/r}, \tag{8}$$

where n_H^{∞} is the interstellar neutral hydrogen density, $n_{\rm SW}^{1\,\rm au}$ is the solar wind density at 1 au, $L_{\rm cav}$ defines the ionization cavity within which minimal pickup ion effects occur, and $\tau_{\rm ion}^{1\,\rm au}$ is the ionization timescale at 1 au. These quantities are reasonably well determined, and we use commonly chosen values for them (see Table 1 and, e.g., B. Breech et al. 2008). Studies that employ Equation (8) have often explored values of $f_D \sim 1/10$ but usually without efforts to determine an optimum f_D (G. P. Zank et al. 1996; W. H. Matthaeus et al. 1999; C. W. Smith et al. 2001; B. Breech et al. 2008; A. V. Usmanov et al. 2011). Hence, this parameter is also a suitable candidate for investigating with Bayesian analysis.

[3] Note that Equation (8) is an approximate model, and more rigorous expressions have been determined and employed in TTMs (P. A. Isenberg et al. 2003; P. A. Isenberg 2005; C. W. Smith et al. 2006a; S. Oughton et al. 2011).

In summary, the TTM parameters that we constrain are α, β, σ_D, f_D, $C_{\rm sh}$, and the BCs at 0.17 au ($Z^2_{0.17}$, $\lambda_{0.17}$, $\sigma_{c,0.17}$, and $T_{0.17}$).[4] As a starting case, we use what we will refer to hereafter as our "nominal" estimates for $\sigma_D = -1/3, f_D = 0.25$, and $C_{\rm sh} = 1.5$ (as used in B. Breech et al. 2008 for example), along with the BCs from the innermost observations, and apply Bayesian analysis to just the α and β parameters (Section 4.1). Following that, we perform extended analyses that also allow determination of posterior distributions for σ_D, f_D, $C_{\rm sh}$, and the BCs (Section 4.2).

2.3. Observational Data

The data we assess against are obtained from in situ observations of the solar wind. The relevant quantities from the data sets are the (traced) rms Elsässer energies $Z^2_{\pm}$, their correlation lengths $\lambda_{\pm}$, the normalized cross helicity σ_c, the normalized energy difference σ_D, and the proton temperature $T_p \equiv T$ (which is the temperature present in Equation (4)). In the inner heliosphere, we make use of Parker Solar Probe (PSP) measurements made between 0.17 and 0.6 au (L. Adhikari et al. 2021). In the outer heliosphere, temperature measurements (C. W. Smith et al. 2006a) and energy and correlation length measurements (L. Adhikari et al. 2015) are from the Voyager 2 mission. To connect the observational values with the TTM variables, we rely on the usual definitions of total energy $Z^2 = (Z^2_+ + Z^2_-)/2$, correlation length $\lambda = (\lambda_+ + \lambda_-)/2$, and normalized cross helicity $\sigma_c = (Z^2_+ - Z^2_-)/(Z^2_+ + Z^2_-)$.

3. Bayesian Analysis Approach

In this section we present an overview of the Bayesian analysis technique and how it is applied to the solar wind TTM, Equations (1)–(4).

For a model $\mathcal{M}$, and a data vector $\mathcal{D}$, we can obtain the probability distributions of model parameters (or sampling parameters) Θ according to Bayes theorem:

$$Pr(\Theta|\mathcal{D}, \mathcal{M}) = \frac{Pr(\mathcal{D}|\Theta, \mathcal{M}) Pr(\Theta|\mathcal{M})}{Pr(\mathcal{D}|\mathcal{M})}, \tag{9}$$

where $Pr(\Theta|\mathcal{D}, \mathcal{M}) \equiv P(\Theta)$ is the *posterior distribution* of the model parameter set. This quantifies the distributions of, and therefore constrains, the sampled parameters Θ given the data and model.

$Pr(\mathcal{D}|\Theta, \mathcal{M}) \equiv \mathcal{L}(\Theta)$ is the *likelihood function* for the data. We use the likelihood function given by

$$\mathcal{L}(\Theta) = (2\pi)^{-N/2} e^{-\chi^2/2} \prod_{i=1}^{N} \sigma_i^{-1}, \tag{10}$$

where N is the number of data points, σ_i is the error associated with each individual data point, and

$$\chi^2 = \sum_{i=1}^{N} \left(\frac{y_i - \tilde{y}_i}{\sigma_i} \right)^2, \tag{11}$$

for observational data[5] y_i and model estimates $\tilde{y}_i$. The likelihood function requires evaluation based on the model predictions given the sampled parameters. In other words, it describes the probability of observing the data $\mathcal{D}$, using the parameters Θ with the model $\mathcal{M}$.

$Pr(\Theta|\mathcal{M}) \equiv \pi(\Theta)$ is the *prior probability distribution* for the model parameter set and can be used to enforce physical knowledge or assumptions into the statistical inferencing. In situations where little is known about the prior one might elect to use a uniform distribution for $\pi(\Theta)$. The particular prior distributions we employ are stated in Section 4.

$Pr(\mathcal{D}|\mathcal{M}) \equiv \mathcal{Z}(\mathcal{D})$ is the Bayesian *model evidence*: the probability of observing the data $\mathcal{D}$, given a model, $\mathcal{M}$. This is a normalizing factor, based on *all* possible Θ values (the space Ω_Θ), and is given by the multidimensional integral

$$\mathcal{Z}(\mathcal{D}) = \int_{\Omega_\Theta} \mathcal{L}(\Theta)\pi(\Theta)\, d^D\Theta, \tag{12}$$

where D is the dimensionality of the parameter space (i.e., the number of model parameters).

To perform our analysis, we make use of the freely available package `pymultinest`[6] (F. Feroz et al. 2009; J. Buchner 2016), a multimodal nested-sampling algorithm (discussed further in Appendix C). This is a Bayesian inference tool that calculates the evidence and produces posterior samples from distributions that may be multimodal, or contain complex degeneracies in high dimensional data.

Currently, we do not have measurements (or estimates) for the error of the data points σ_i. We therefore assume the error is constant and the same for all data points (i.e., $\sigma_i = k$ is constant), and obtain an unnormalized likelihood function by setting $k = 1$. Instrumental errors are assumed to have minimal effect on the variables Z^2, λ, σ_c, σ_D, and T due to the considerable averaging of data that is performed in obtaining binned radial estimates. Ideally, we would have error bars for each variable in each radial bin, based on variation of repeated samplings, or inherent in the randomness of turbulence in the solar wind. Overall, more work needs to be done to obtain statistical errors, based on variations over repeated/averaged samplings of solar wind data for all relevant variables represented in the models. For example, recent work (M. E. Cuesta et al. 2022a) reporting the standard deviations for binned correlation lengths, λ, could be incorporated in future Bayesian analyses.

For each selection of parameters Θ (such as α, β, etc.), the Bayesian analysis calls the numerical setup (Section 3.1), which solves the model system and returns the radial solutions for variables $Z^2(r)$, $\lambda(r)$, $\sigma_c(r)$, $T(r)$, and if configured, constant σ_D[7] (see Equation (7)). These numerical solutions ($\tilde{y}_i$) are then used in tandem with the observational data (y_i) to calculate the χ^2 values. The `pymultinest` code runs until the evidence estimate has converged, and yields the samples of the posterior distribution, with their weights, based on the likelihood and prior values. Using these samples, we can generate estimates for the posterior distributions and also calculate confidence intervals about the means of the distributions of solutions contained in the posterior samples. The obtained posterior distributions are (N-dimensional) joint posteriors, and pairs of dimensions can be visualized using 2D contours. Some specific

[4] In general, Bayesian analysis can be used to constrain any parameter in a TTM.

[5] Since the data spans many orders of magnitude, we found it useful to take the base-10 log of the data y_i and the model estimate $\tilde{y}_i$ before calculating the χ^2. This helps avoid prioritizing one set of parameter observations over another. Consequently, although we do not calculate the true χ^2, the quantity we do calculate plays an analogous role.

[6] https://github.com/JohannesBuchner/PyMultiNest

[7] To keep the number of degrees of freedom the same across our different analyses, we need to ensure that the number of elements in the χ^2 summation is always the same. We therefore include the $\sigma_D(r) = \text{const}$ comparison to σ_D observations in all analyses, including ones where we set $\sigma_D = -1/3$.

2D joint-posterior distributions are discussed in Section 5. In cases where the sampled parameters are weakly correlated, it can be appropriate to view just the 1D distributions.

In order to decide on an appropriate model to use, it is helpful to compare different models with statistical rigor. This can be achieved by evaluating the model evidence $\mathcal{Z}(\mathcal{D})$; see Equation (12). Since $\mathcal{Z}(\mathcal{D})$ is the integral of the prior-weighted likelihood over the entire parameter space, it describes the overall effectiveness of the model. The $\mathcal{Z}(\mathcal{D})$ protects against overfitting by penalizing posteriors that cover large fractions of the prior space, and naturally favors simpler models, unless the likelihood is vastly improved. Two models, 1 and 2, may be compared using the Bayes factor, which is essentially the ratio of their model evidences; the model with the largest $\mathcal{Z}(\mathcal{D})$ is most favored. For large values of the model evidences, it may be more practical to instead work with $\ln \mathcal{Z}_1 - \ln \mathcal{Z}_2$. Note that, since we have essentially assumed no error in the observations, the model evidences are not a completely fair description; however, since the Bayes factor is the ratio of two evidences with the same error assumptions, the results should be defensible.

3.1. Numerical Setup

We solve the system (Equations (1)–(4)) numerically using LSODA (L. Petzold 1983) for r from 0.17 to 80 au,[8] with a minimum step size of 1 km. The Python `scipy` implementation of LSODA, `solve_ivp()`, supports an automatic halting of solving the system. This is an advantageous feature as we may encounter combinations of sampled parameters for which the TTM is not easily solvable. In such cases, we flag a bad parameter selection for `multinest`.

4. Results

We carry out several Bayesian/`multinest` analyses of the available models, beginning with the smaller analyses that constrain only the vKH α–β parameters, named the α–β analysis. Next, we perform an analysis that includes most of the other model parameters, which are constant (but not precisely determined), specifically σ_D, f_D, and $C_{\rm sh}$. This is referred to as the α–β–σ_D–f_D–$C_{\rm sh}$ analysis. Analyses with respect to the BCs for the four transported quantities ($Z^2_{0.17}$, $\lambda_{0.17}$, $\sigma_{c,0.17}$, and $T_{0.17}$), treating them as parameters with distributions to constrain, are also performed. These can be useful when the boundary values are unknown and/or display observational scatter. This latter approach may also capture more of the scatter present in the larger radii solar wind observations.

Two other analyses are also executed. The first showcases constraining the model parameters using split data sets. This enables examination of how the different data sets contribute to the constraints on the sampled parameters. Lastly, we investigate the effects of removing the PI driving term from the λ evolution equation.

[8] The termination shock has been observed at $r \gtrsim 84$ au (e.g., D. McComas et al. 2019) where, there and beyond, our TTM is unlikely to be applicable since it does not include interaction of the solar wind with the local interstellar medium. Note that the choice of $r_{\rm max} = 80$ au for the maximum radius is essentially a cosmetic one. Provided $r_{\rm max}$ is greater than the distance of the last observational data point, it has no effect on the Bayesian results. This is because the χ^2 values (Equation (11)) are calculated by comparing the data and the model only at the distances where we have observational values (we use data up to 75 au).

Table 2
Prior Distributions of the α and β vKH Parameters Used in the Bayesian Analysis of the 2D and 3D TTMs

Parameter	Prior Distribution
α	$\mathcal{U}[0.01, 2]$
β	$\mathcal{U}[0.01, 2]$

Note. $\mathcal{U}[\cdot,\cdot]$ denotes a uniform distribution with the arguments indicating the domain boundaries.

Table 3
Inner Boundary Values Employed When These Parameters Are Assigned δ-function Priors (i.e., Kept Fixed) in the Bayesian Analysis

Quantity	Value
$Z^2_{0.17}$	7040 $(\mathrm{km\ s^{-1}})^2$
$\lambda_{0.17}$	55,400 km
$\sigma_{c,0.17}$	0.81
$T_{0.17}$	232,000 K

Note. Values are approximately those from PSP data presented in L. Adhikari et al. (2015).

4.1. α–β Analysis

In this section, we perform what are our smallest analyses for the 2D and 3D TTMs, searching only over α and β. As priors for α and β, we use the uniform distributions stated in Table 2, where the intention is to cover as much of the parameter space as possible without influencing the posterior distribution, that is, we are keeping the priors as uninformative as possible. The inner boundary values, $Z^2_{0.17}$, $\lambda_{0.17}$, $\sigma_{c,0.17}$, $T_{0.17}$, are fixed and based on PSP observations at $r_0 \approx 0.17$ au, as reported in L. Adhikari et al. (2015). See Table 3.

If we had error estimates for the observational data points, we would approximate a posterior predictive distribution (PPD), and use it to understand how well the model fits the data. A PPD describes the distribution of possible unobserved values. That is, it takes into account the uncertainties of the mean of the posterior distribution for the TTM parameters, as well as the uncertainties in the observations to calculate the probabilities of future observations. A PPD would be a rigorous way of using a TTM to predict future measurements of the solar wind as a function of heliocentric radius.

Since, however, we do not have estimates for the errors in the data points (we are neglecting all forms of uncertainty in the observations), the PPDs are not able to be calculated. In Figure 1, we instead display the predicted radial distribution of $Z^2(r)$, $\lambda(r)$, $T(r)$, and $\sigma_c(r)$ based on the mean of the estimated posterior distribution, $P(\Theta)$, of the constrained parameters Θ in the TTM. The uncertainties associated with these predictions[9] are characterized by the confidence intervals and displayed using contours of the 1σ, 2σ, and 3σ deviations. These contours are calculated by solving the TTM for each parameter's posterior sample. We can then calculate the mean, and confidence intervals, given the range of these TTM solutions provided for each radial distance. *If* the uncertainties in the parameters Θ (as described by the estimated posterior distributions) are expected to describe the scatter in the

[9] We emphasize again that these confidence interval uncertainties do not necessarily capture the full uncertainty associated with the observations.

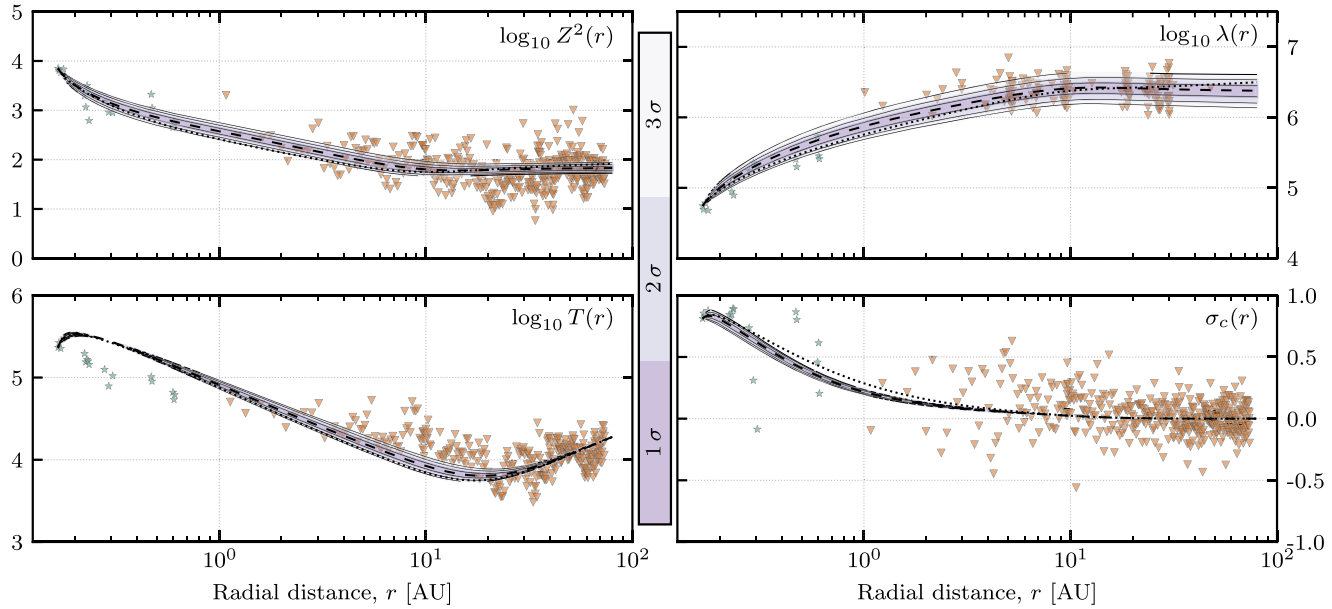

Figure 1. Solutions of the α–β Bayesian analysis. The posterior sampled means for the 2D and 3D TTMs are plotted as dashed and dotted black lines respectively. Solid lines depict the 1σ, 2σ, and 3σ confidence interval contours in the means of the 2D TTM solutions. The latter are determined using the sampled posterior distributions for the (2D TTM) α–β analysis. Green stars indicate *PSP* data points, and orange triangles Voyager 2 data points. Units are as in Table 3.

observations, we would expect the confidence intervals to cover most (if not all) of the observed data points.

From Figure 1, it is evident that overall the solutions match the data reasonably well, although the scatter in the observations is not completely captured (except for $\lambda(r)$, which describes the data well). The qualitative behavior of $T(r)$ accords with the expected evolution: slower than the adiabatic $r^{-4/3}$ profile, with an increase at large radial distances due to the PI driving. However, the $T(r)$ solutions show an unphysical increase in temperature near the inner boundary ($0.17 < r < 0.2$). Furthermore, they exhibit values systematically larger than the PSP observational data at small radial distances, and smaller than the bulk of Voyager 2 data at intermediate radial distances ($r \sim 10$ au). Notably, the $\sigma_c(r)$ solutions are all very similar, lying almost on top of each other, and quickly converge toward $\sigma_c = 0$ with increasing r. This is distinctly different from the observational data that is scattered between approximately ± 0.5 beyond $r \approx 1$ au. This scatter is expected to be from variability in the solar wind turbulence rather than due to the effects of observational noise.

4.2. Analyses Including σ_D, f_D, C_{sh}, and Boundary Conditions

In the previous subsection, we carried out Bayesian analysis allowing just the α and β TTM parameters to vary. Here, we extend the analysis so that all five of the adjustable parameters in the TTM, plus the inner BCs, are allowed to vary. In addition to this "full" analysis, we also assess several subcases where only some of the model parameters and/or BCs are analyzed over. The three combinations we investigate are

(i) α–β–BC,
(ii) α–β–σ_D–f_D–$C_{\rm sh}$,
(iii) α–β–BC–σ_D–f_D–$C_{\rm sh}$,

and for each of these, the 2D and 3D TTMs are assessed. The extended analyses require sampling more of the TTM parameters, and therefore more evaluations of χ^2, which increases the code run times. In our case, the analyses are still acceptably quick to compute even when run on a reasonably standard desktop computer (Appendix C).

Table 4
Prior Distributions Employed in the Analyses That Include the BCs (Top Half) and the Constant TTM Parameters (Lower Half)

Quantity	Prior Distribution
$Z^2_{0.17}$	$\mathcal{U}[10^2\ (\mathrm{km\ s^{-1}})^2,\ 10^5\ (\mathrm{km\ s^{-1}})^2]$
$\lambda_{0.17}$	$\mathcal{U}[10^3\ \mathrm{km},\ 10^7\ \mathrm{km}]$
$\sigma_{c,0.17}$	$\mathcal{U}[0,\ 1]$
$T_{0.17}$	$\ln\mathcal{N}(2.5 \times 10^5\ \mathrm{K},\ 0.5)$
σ_D	$\mathcal{U}[-1,\ 1]$
f_D	$\mathcal{U}[0.01,\ 1]$
$C_{\rm sh}$	$\mathcal{U}[0.01,\ 8]$

Note. The priors for α and β are stated in Table 2. $\mathcal{U}[\cdot,\cdot]$ denotes a uniform distribution with the arguments indicating the domain boundaries, and $\ln\mathcal{N}(\mu,\ \sigma)$ denotes a log-normal distribution with location parameter μ and logarithm of scale parameter σ.

The α–β–BC case includes the BCs—$Z^2_{0.17}$, $\lambda_{0.17}$, $\sigma_{c,0.17}$, and $T_{0.17}$—as parameters to constrain. Their prior distributions are described in the top section of Table 4, with the α and β priors still given by Table 2. We choose the BC priors to be as uninformative as possible, namely, uniform for $Z^2_{0.17}$, $\lambda_{0.17}$, and $\sigma_{c,0.17}$, and a log-normal distribution for $T_{0.17}$. The mean and variance for the $T_{0.17}$ prior were chosen to accord with the innermost Helios observations discussed in P. Hellinger et al. (2013). We remark that, when a uniform prior for $T_{0.17}$ was investigated, we found the resulting posterior distribution had a large tail extending toward unreasonably small values. Allowing the BCs to have distributions makes some allowance for the nonsteady nature of the solar wind observations. For example, observed values at 5 and 10 au typically will not correspond to the same parcel of solar wind transported from $r = 0.17$ au.

For the α–β–σ_D–f_D–$C_{\rm sh}$ case, the analysis is essentially the same as that used for the α–β case discussed in Section 4.1, but

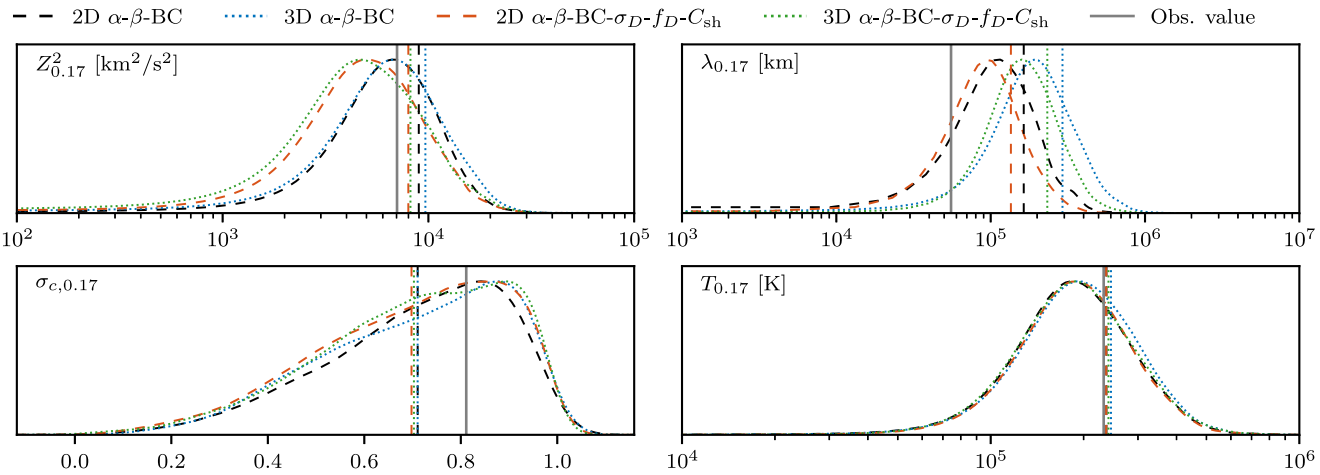

Figure 2. 1D posterior distributions of the 2D (dashed) and 3D (dotted) models of the α–β–BC and α–β–BC–σ_D–f_D–$C_{\rm sh}$ analyses. Vertical lines with the same linestyle and color represent the mean value of the sampled posterior distributions. For comparison, the vertical gray line is the PSP innermost observation, used in the analyses that do not constrain these variables (α–β, and α–β–σ_D–f_D–$C_{\rm sh}$); see Table 3.

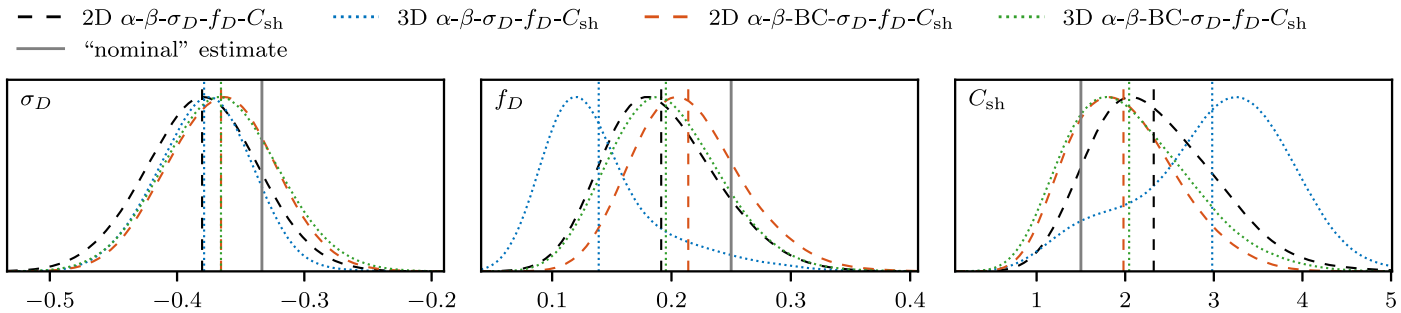

Figure 3. The 1D posterior distributions of σ_D (left), f_D (middle), and $C_{\rm sh}$ (right) for the 2D and 3D TTMs (dashed and dotted) of the α–β–σ_D–f_D–$C_{\rm sh}$ and α–β–BC–σ_D–f_D–$C_{\rm sh}$ analyses. The vertical lines represent the mean value of the respective plotted sampled posterior distributions. For comparison, the vertical gray lines are the assumed values for the analyses that do not constrain these variables (α–β, and α–β–BC); see Table 1.

with the inclusion of the other adjustable parameters: σ_D, f_D, and $C_{\rm sh}$. We employ uniform priors for these, as listed in the second section of Table 4 (and Table 2), once again keeping them as nonrestrictive as possible within the range of reasonable expected values. Note that the uniform prior for $C_{\rm sh}$ is extended compared to the 0–2 range of values described by B. Breech et al. (2008).

The third case, α–β–BC–σ_D–f_D–$C_{\rm sh}$, contains all the parameters described thus far, using the priors already stated (Tables 2 and 4).

Figure 2 displays the 1D posterior distributions for the BCs obtained from both the α–β–BC analysis and the α–β–BC–σ_D–f_D–$C_{\rm sh}$ analysis, cases (i) and (iii). Results are shown for the 2D and 3D TTMs. The vertical lines show the mean value of the respective posterior distributions. These mean values may be treated as corresponding to the "best" solutions. Considering the visually simplest distribution first, the $T_{0.17}$ (bottom right) posterior distributions are essentially identical, with mean values that align well with the *PSP* observation. Similarly, the $\sigma_{c,0.17}$ (bottom left) posterior distributions for the different analyses are similar, resulting in mean values of $\sigma_{c,0.17} \approx 0.7$, slightly smaller than the observational value of $\sigma_{c,0.17} \approx 0.8$. For a given case—(i) or (iii)—the $Z^2_{0.17}$ (top left) 1D posterior distributions are very similar for the two TTMs (i.e., the 2D and 3D models). The mean is slightly larger for the α–β–BC analyses. Although the $Z^2_{0.17}$ PSP observation is smaller than the mean sampled posterior values, the posterior distributions are consistent with the observational value. The situation for $\lambda_{0.17}$ (top right) is switched relative to that for $Z^2_{0.17}$, with the posteriors for the 2D TTM being similar across cases (rather than across TTM models), and likewise for the 3D TTM posteriors, although with these shifted to larger values. The resulting mean of the sampled posterior distribution for the 3D α–β–BC analysis is almost an order of magnitude larger than the PSP observation. The observed value is still consistent with the $\lambda_{0.17}$ posterior distributions, but only marginally so for the 3D models.

Figure 3 presents 1D posterior distributions from cases (ii) α–β–σ_D–f_D–$C_{\rm sh}$ and (iii) α–β–BC–σ_D–f_D–$C_{\rm sh}$, once again for both the 2D and 3D TTMs so that there are four different distributions on each panel. Shown are the posteriors for σ_D, f_D, and $C_{\rm sh}$.

For σ_D, the four posterior distributions are quite similar and consistent with the commonly used (and observationally based) value of $\sigma_D \approx -1/3$ (S. Perri & A. Balogh 2010). The α–β–σ_D–f_D–$C_{\rm sh}$ analysis has mean values of $\sigma_D \approx -0.38$, and the α–β–BC–σ_D–f_D–$C_{\rm sh}$ has mean values of $\sigma_D \approx -0.36$. Moving on to the f_D distributions, these are similar for the (2D and 3D) α–β–BC–σ_D–f_D–$C_{\rm sh}$ analysis and just the 2D α–β–σ_D–f_D–$C_{\rm sh}$ analysis. Most of the mean values are $f_D \approx 0.2$, slightly smaller than the nominal value of $f_D \approx 0.25$. The exception is for the 3D α–β–σ_D–f_D–$C_{\rm sh}$ analysis, for which the posterior distribution and the mean $f_D \approx 0.12$ are both quantitatively distinct from the other cases.

Examining the $C_{\rm sh}$ posterior distributions, we see that they extend well past the $C_{\rm sh} \in \mathcal{U}[0, 2]$ range assumed in

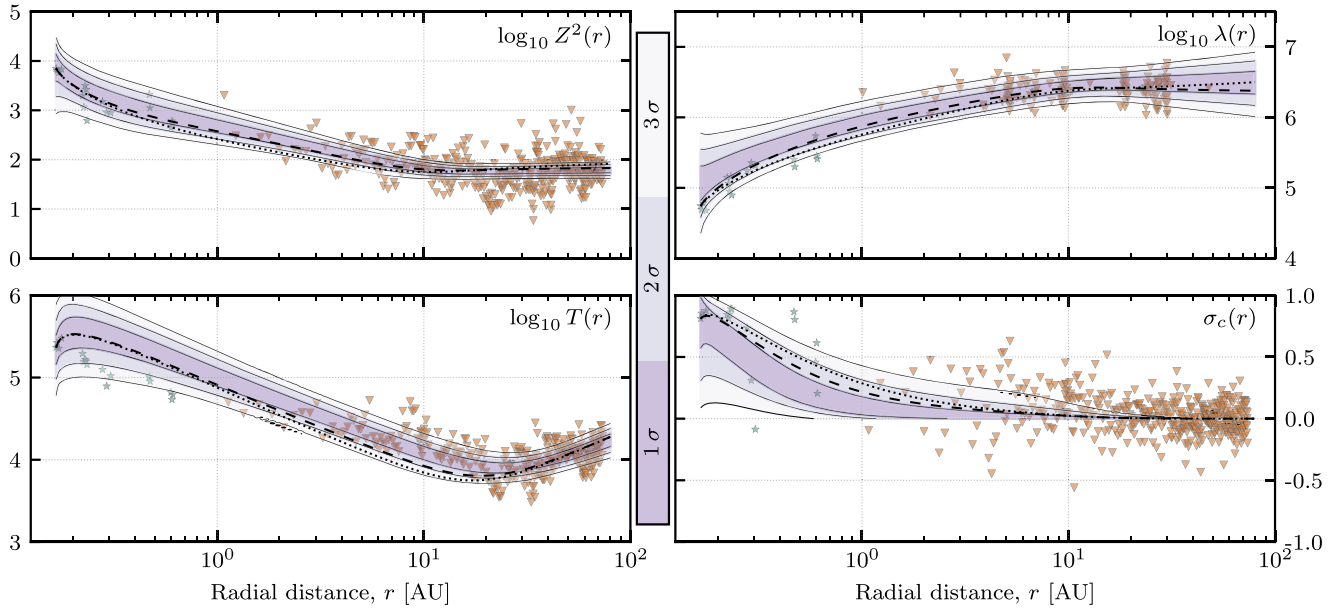

Figure 4. Solutions for the 2D α–β–BC–σ_D–f_D–$C_{\rm sh}$ analysis. The contours represent the confidence intervals of the means in the solutions obtained by the sampled posterior distributions. Green stars show the PSP data, and the orange triangles the Voyager 2 data. The 2D and 3D TTM posterior sampled means of the α–β analysis are plotted with dashed, and dotted black lines respectively. Units are as in Table 3.

B. Breech et al. (2008), motivating our use of an extended range for the prior. Without extending the prior, the obtained posterior distributions would be unnaturally constrained against the $C_{\rm sh} = 2$ wall. All of the mean values are larger than the nominal value of $C_{\rm sh} \approx 1.5$ (Table 1). For the 2D and 3D α–β–BC–σ_D–f_D–$C_{\rm sh}$ analyses, the means are $C_{\rm sh} \approx 2$, values that are not in tension with $C_{\rm sh} = 1.5$ given the widths of the distributions. Once again, the 3D α–β–σ_D–f_D–$C_{\rm sh}$ analysis shows a distinct distribution compared to the other results, and an even larger mean value of $C_{\rm sh} \approx 3$. The extended range of the $C_{\rm sh}$ prior and posterior distributions are considered further in Section 4.3.

Figure 4 shows confidence intervals for the 2D case (iii) α–β–BC–σ_D–f_D–$C_{\rm sh}$ analysis. For comparison, the solutions shown in Figure 1 (i.e., using the mean sampled posterior values for the 2D and 3D α–β analysis) are also included. See Appendix C for the confidence intervals of σ_D for this same analysis case.

We can see that the inclusion of the additional parameters (and the BCs) in the Bayesian analysis leads to confidence intervals that span a greater range of values. In other words, there is more uncertainty associated with the "best" TTM solution. If the confidence interval contours were to cover the majority (or all) of the scatter in the observations, this greater uncertainty could be considered advantageous since it supports explaining the scatter in the data as variability in the solar wind caused by non-steady-state behavior.

The range in the $Z^2(r)$, $\lambda(r)$, $T(r)$, and $\sigma_c(r)$ solutions has increased, compared to the α–β analysis, allowing them to capture much more of the observational scatter. We still see the unphysical increase in $T(r)$ close to the inner boundary, and indeed, it is present in all of the $T(r)$ confidence intervals. Additionally, the $T(r)$ confidence intervals typically cover a wider range than the PSP observational data do. However, on the plus side, compared to the α–β analysis, $T(r)$ captures much more of the observed Voyager 2 observations. For σ_c, we see that the confidence intervals are wide at smaller radial distances, but converge to $\sigma_c = 0$ with increasing distance. The scatter in the σ_c observations is not well captured.

Note that the mean solutions from the 2D α–β analysis tend to lie within the 1σ or 2σ confidence intervals for the α–β–BC–σ_D–f_D–$C_{\rm sh}$ analysis.

As the confidence intervals indicate, the nonsteady state and variation of parameters allowed by the 2D α–β–BC–σ_D–f_D–$C_{\rm sh}$ analysis are able to capture some of the scatter in the observations. However, the additional parameters are not completely sufficient to model all of the scatter in the observations, particularly for Z^2 and σ_c at large radial distances.

4.3. Split Data Set Analysis

Our observational data come from two separate spacecraft missions, PSP (<1 au) and Voyager 2 (>1 au). To check for consistency and biases, we repeated the Bayesian analysis using just one data set at a time and compared the individual results to each other, and to the combined data set analysis presented in the previous section. The results obtained (not shown) are consistent with those discussed in the rest of this section.

Separate data set analyses could provide independent indications of the effect of the "inner" heliosphere data on the whole TTM model and of the "outer" heliosphere data on the whole TTM model. Alternatively, we could investigate splitting the data based on relevant physical differences that apply inside and outside an appropriate distance. We report on this second option below, choosing the splitting distance to be 5 au. This distance is a little smaller than the radius of the PI ionization cavity, $L_{\rm cav} = 8$ au, and a little larger than the distance where large-scale stream shear is strongest in the inner heliosphere.

We show the split data sets (split at 5 au) using all of the available parameters, i.e., α–β–BC–σ_D–f_D–$C_{\rm sh}$ with the 2D model. For both portions of the split (<5 au, and >5 au), and for the joint data set (i.e., the 2D α–β–BC–σ_D–f_D–$C_{\rm sh}$ analysis in Section 4.2), the model is solved from the inner radius

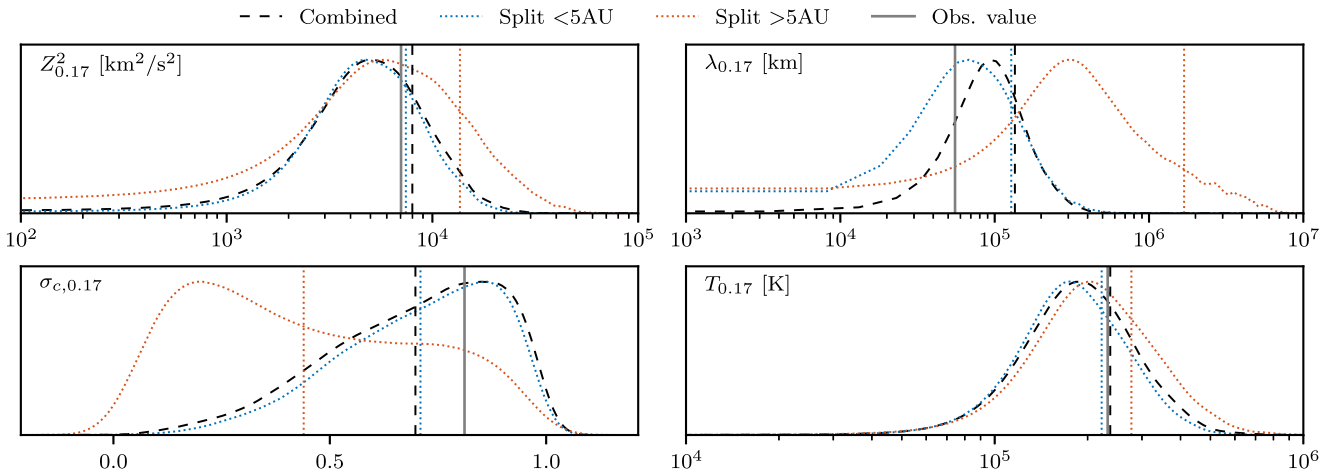

Figure 5. 1D posterior distributions for the 2D model α–β–BC–σ_D–f_D–$C_{\rm sh}$ analyses using split data sets: <5 au (dotted blue), and >5 au (dotted orange), and the combined data set (dashed black). Vertical lines represent the mean value of the sampled posterior distributions. For comparison, the vertical gray line is the PSP innermost observation, used in the analyses that do not constrain these variables (α–β and α–β–σ_D–f_D–$C_{\rm sh}$); see Table 3.

$r_0 = 0.17$ au to $r_{\rm max} = 80$ au. The only difference is the data we are including in the likelihood evaluation (Section 3).

Figure 5 shows the 1D posterior distributions for the BCs of the 5 au split data set analyses along with the already presented combined analysis of Section 4.2. We obtain consistent posterior distributions for $T_{0.17}$ for both splits. For σ_c, the <5 au analysis is consistent with the combined analysis, whereas the >5 au analysis gives a very unconstrained posterior distribution, favoring the smaller values. This is expected due to the roughly symmetric spread about zero in the Voyager 2 σ_c data set for $r > 5$ au. It is also expected that the <5 au data set contributes the most to the joint analysis (evidenced by the identical distributions) because it is the BCs that correspond to the inner-heliosphere observations. Similarly, the inner-heliosphere analysis constrains $Z^2_{0.17}$ (again, identical distributions). The outer-heliosphere posteriors are also consistent with the inner-heliosphere posteriors but with slightly larger mean values. For $\lambda_{0.17}$, the outer-heliosphere posterior is broad, with a mean much larger than those for the inner-heliosphere and the combined analysis. The combined analysis is influenced by both data sets, but predominantly the <5 au data set. Overall, there is no substantial disagreement between the posteriors for $Z^2_{0.17}$, $\lambda_{0.17}$, $\sigma_{c,0.17}$, and $T_{0.17}$ obtained from the three data sets (combined, <5 au, and >5 au).

Figure 6 shows the 1D posterior distributions for σ_D, f_D, and $C_{\rm sh}$. The inner-heliosphere data set for σ_D yields a less constrained posterior distribution compared to those for the other two cases, which are rather tightly peaked near $\sigma_D \approx -1/3$. This indicates that it is the outer-heliosphere data set that is controlling the behavior for the combined data set. The mean values for the two split data sets are similar and consistent with the combined analysis, and with the assumption of $\sigma_D \approx -1/3$ used in the simplest (α–β) analysis. Expectedly, the inner-heliosphere data set shows an unconstrained result for f_D, as the PI driving term is near zero at $r < 5$ au, due to the exponential factor in Equation (8). The $C_{\rm sh}$ TTM parameter constraints are significantly different for the inner- and outer-heliosphere data sets. The outer-heliosphere posterior is relatively narrow and spans the value range of [0, 2], as discussed by B. Breech et al. (2008). The inner-heliosphere posterior is less constrained and extends well past $C_{\rm sh} = 2$. This is the cause of the combined data analysis results, as introduced in Section 4.2. The inner-heliosphere data set requires a considerably larger value of $C_{\rm sh}$, and this value predominates in the combined analysis. This accords with expectations that shear driving is stronger in the inner heliosphere, since large-scale velocity gradients tend to decrease with heliocentric distance (e.g., Y. Zhou & W. H. Matthaeus 1990; R. Bruno & V. Carbone 2013). However, this result also suggests that the use of $C_{\rm sh} = $ const is not adequate to properly capture the solar wind dynamics over a large range of distances. Although note, these $C_{\rm sh}$ results are within $\approx 1\sigma$ of each other, so there is no statistically significant disagreement.

Thus, overall, we find no fundamental disagreement between the posterior distributions obtained from the individual data sets and from the combined data sets. The posterior distributions obtained for each split data set mostly show significant overlap with the posteriors for the combined data set. This indicates that the Bayesian constraints are not being distorted or biased, given our current TTM, by (known or unknown) observed features of the solar wind. The inclusion of more data correctly serves to improve the Bayesian constraints and does not provide any conflict to our results.

4.4. No Pickup Ion Driving of λ

Equation (2) for the turbulence correlation length λ contains a term involving $\dot{E}_{\rm PI}$. This arises via imposition of the local conservation law $Z^{2\beta/\alpha}\lambda$ (just for the pickup ion effects) and its implication that

$$\left.\frac{d\lambda}{dr}\right|_{\rm PI} = -\frac{\beta}{\alpha}\frac{\lambda}{Z^2}\left.\frac{dZ^2}{dr}\right|_{\rm PI}, \tag{13}$$

where $\frac{d\cdot}{dr}|_{\rm PI}$ indicates the contribution to the evolution equation from just the pickup ion driving (G. P. Zank et al. 1996; W. H. Matthaeus et al. 1999).

Recall, however, that PI driving is expected to directly modify only the parallel length scale of the turbulence, and at scales of order the ion gyroradius, which is much smaller than the turbulence correlation length λ (e.g., M. Lee & W.-H. Ip 1987; P. A. Isenberg et al. 2003). Unfortunately, this physics is not accurately described in the TTMs considered here, since these evolve a single characteristic lengthscale, λ, that is both

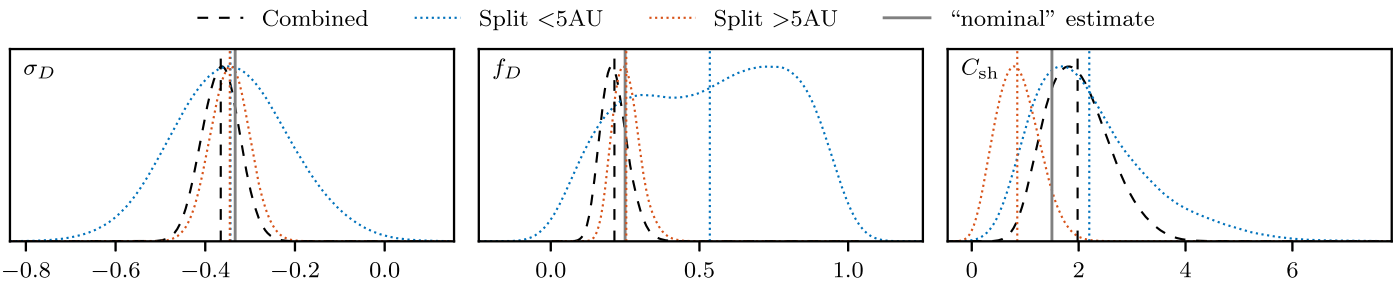

Figure 6. 1D posterior distributions of σ_D (left), f_D (middle), and $C_{\rm sh}$ (right) for the 2D model α–β–BC–σ_D–f_D–$C_{\rm sh}$ analyses using the <5 au data set (dotted blue), the >5 au data set (dotted orange), and the combined data set (dashed black). For comparison, the vertical gray lines are the values imposed for the analyses that do not constrain these variables; see Table 1.

"large" scale and essentially a perpendicular rather than a parallel scale (see, e.g., S. Oughton et al. 2011; J. M. Sokół et al. 2022; E. J. Zirnstein et al. 2022). Thus, it is not a priori clear whether or not it is advantageous to include PI effects in the λ equation, as far as agreement with observational data is concerned.

To investigate this, we consider modified forms of the TTMs that *exclude* the PI driving term in the λ evolution equation, which is thus replaced with

$$U\frac{d\lambda}{dr} = \frac{\lambda\sigma_D M_\lambda U}{r} + \beta f^+(\sigma_c)Z. \tag{14}$$

We refer to these as "no λ PI" TTMs, to be contrasted with the "standard" TTMs associated with Equations (1)–(4). (Throughout this paper, references to a specific analysis, e.g., α–β–BC, are to be interpreted as meaning that the TTM uses Equation (2), unless we explicitly state that it instead uses Equation (14).)

We may then perform Bayesian analyses of the two situations, using the same setup as in Sections 4.1 and 4.2 and with priors as given in Tables 2 and 4. The results indicate that the "no λ PI" TTM models typically give worse agreement with the observational data than those employing Equation (2). Table 5 lists the log-evidences for these cases, and this will be discussed further in Section 5.

Table 5
The Bayes Factors, $\ln K = \ln \mathcal{Z}_{\rm model} - \ln \mathcal{Z}_{\rm fiducial}$, for the 2D and 3D Models for the Various Analyses Discussed in Section 4

Analysis	2D Model	3D Model
α–β	0.00	−5.40
α–β–BC	−5.41	−6.54
α–β–σ_D–f_D–$C_{\rm sh}$	−4.35	−9.57
α–β–BC–σ_D–f_D–$C_{\rm sh}$	−10.61	−11.48
α–β	−32.97	−42.11
α–β–BC	−16.75	−16.03
α–β–σ_D–f_D–$C_{\rm sh}$	−9.70	−11.97
α–β–BC–σ_D–f_D–$C_{\rm sh}$	−15.44	−16.30

Note. We subtract the fiducial model log-evidence, chosen as that for the 2D α–β analysis, from each model log-evidence. The lower section of the table provides the Bayes factors for the TTMs *without* the PI term in the λ evolution equation (Section 4.4), using the same 2D α–β fiducial model employed in the top section.

5. Discussion

5.1. Joint-posterior Distributions and Their Correlations

Typically, results from solar wind TTMs have been presented using one, or a few, hand-picked values for the adjustable parameters. The Bayesian analysis techniques explored in this study improve on that situation by enabling study of the distributions of these parameters and illumination of their interrelations. The posterior samples obtained by the Bayesian analysis allow us to do so by analyzing the joint-posterior distributions of the variables of interest.

5.1.1. α–β Correlation

Figure 7(a) shows the α–β joint-posterior distributions for the 2D model analyses described in Section 4. Although the TTMs have forcing terms, one might wonder if these α–β correlations will nonetheless display behavior related to the conservation laws inherent in vKH modeling for decaying homogeneous turbulence (M. Hossain et al. 1995; W. H. Matthaeus et al. 1996b), i.e., $\lambda Z^{2\,\beta/\,\alpha} = \text{const}$. Particular values of the ratio $m = \alpha/\beta$ correspond to some well-known turbulence models; for example, decay at constant Reynolds number ($m = 2$), the P. G. Saffman (1967) model ($m = 3$), and the A. N. Kolmogorov (1941) model ($m = 5$), which all yield straight lines in the α–β plane. To test this, we plot in Figure 7(b) the constrained straight lines of best fit calculated using the weighted posterior samples. For comparison, we include specific pairs of α–β values that have been used in the literature (C. Pei et al. 2010; A. V. Usmanov et al. 2014; J. Kleimann et al. 2023). We note that these literature values are not directly intercomparable since the various studies typically use different TTMs (which could influence the posterior distributions of the α–β parameters). Other studies often employed $\alpha = 2\beta$, but with $\beta \gtrsim 0.2$ so that the values are off-scale in Figure 7 (e.g., B. Breech et al. 2008; L. Adhikari et al. 2015, 2017a, 2017b, 2021).

Clearly, the joint-distributions show strong positive correlations, particularly for the α–β and α–β–BC analyses. Indeed, the latter (where uncertainty in the BCs is allowed for) strongly follows the $\alpha = 2\beta$ correlation. For homogeneous freely decaying hydrodynamic turbulence, this would be consistent with an approximately constant Reynolds number (see W. H. Matthaeus et al. 1996b). However, the TTM models we analyze herein have shear and PI forcing, and this alters expectations for the radial evolution of the Reynolds number (G. P. Zank et al. 1996). Furthermore, observation-based estimates for (equivalent) Reynolds numbers for the solar wind have been shown to have considerable variability, both at 1 au and as a function of heliocentric distance (T. N. Parashar et al. 2019; M. E. Cuesta et al. 2022b; D. Wrench et al. 2024). Thus, the reasons for an $\alpha = 2\beta$ correlation are likely to be more

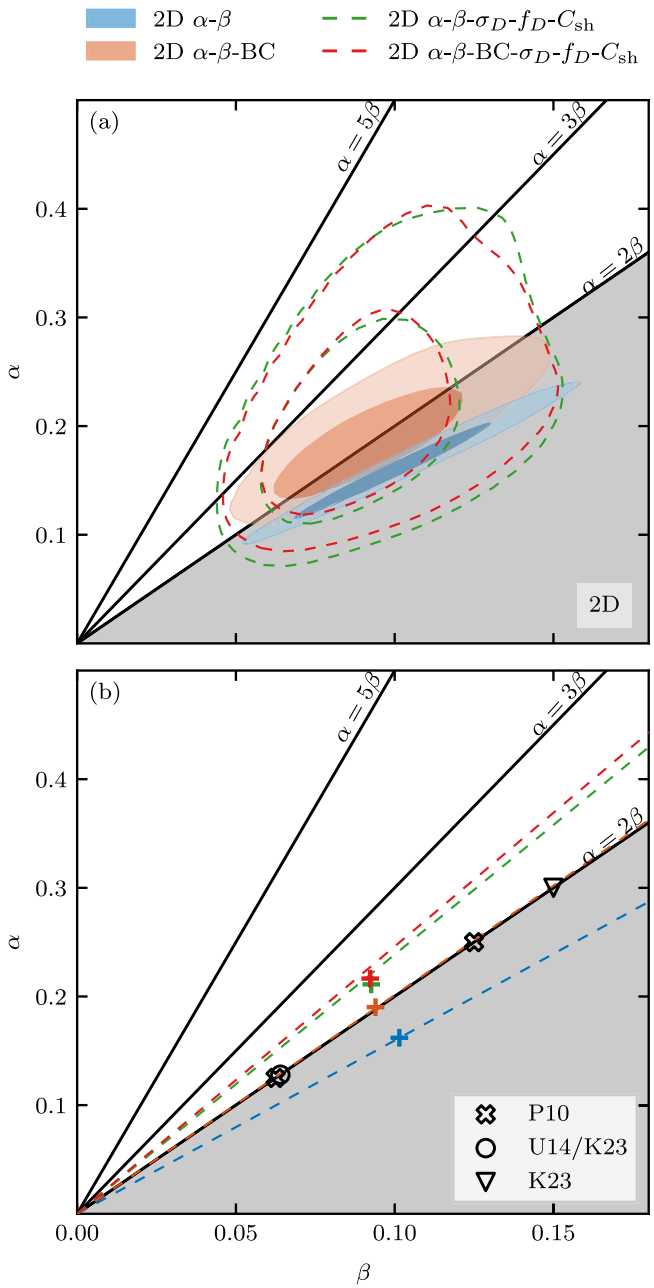

Figure 7. (a) 68% and 95% intervals of the joint α–β posterior distributions for the 2D TTM for several Bayesian analysis cases: α–β (blue contours), α–β–BC (orange contours), α–β–σ_D–f_D–$C_{\rm sh}$ (green dashed), and α–β–BC–σ_D–f_D–$C_{\rm sh}$ (red dashed). (b) The corresponding constrained linear relations (dashed lines of the same color) fitted to the weighted joint-posterior samples, with colored crosses representing the means. Some specific α–β pairs that have been used in the literature are also shown: P10 (C. Pei et al. 2010), U14 (A. V. Usmanov et al. 2014), and K23 (J. Kleimann et al. 2023). In both panels, the black lines represent $\alpha = m\beta$ relations, corresponding to the physical implications associated with constant Reynolds number ($m = 2$), Saffman's model ($m = 3$), and Kolmogorov's model ($m = 5$). The shaded region, $\alpha \leqslant 2\beta$, indicates values that imply the Reynolds number increases with heliocentric distance; these would be unphysical for purely decaying turbulence.

complicated than those holding in simpler decaying hydrodynamic situations.

Extending the analysis to include the parameters σ_D, f_D, and $C_{\rm sh}$ yields 68% intervals that lie largely in the region in between $\alpha = 2\beta$ and $\alpha = 3\beta$, with slightly steeper constrained linear relations ($\alpha \approx 2.38\beta$). Clearly, the interval contours are significantly broader than those for the α–β and α–β–BC analyses and could be considered a superset of them. The α–β analysis has a shallower slope ($\alpha = 1.59\beta$), and the entire distribution lies below the $\alpha = 2\beta$ line. Recall that for freely decaying homogeneous turbulence that line corresponds to a vKH phenomenology evolution where the Reynolds number is constant (H. L. Dryden 1943; W. H. Matthaeus et al. 1996b). Moreover, α–β pairs lying below that line would correspond to dynamics with an increasing Reynolds number, which is unphysical for undriven turbulence. However, in the TTMs we consider, driving is present, and the $\alpha < 2\beta$ region is not necessarily forbidden, and the overall picture can be significantly more complex (see T. N. Parashar et al. 2019, Figure 1).

Figure 8 is the equivalent of Figure 7(a) but for some of the other analyses discussed in Section 4. The 3D model analysis α–β results (panel (a)) share some similar behavior, with constrained fitted linear correlations: $\alpha = 1.75\beta$, $\alpha = 2.70\beta$, $\alpha = 3.33\beta$, $\alpha = 3.33\beta$ for the α–β, α–β–BC, α–β–σ_D–f_D–$C_{\rm sh}$, and α–β–BC–σ_D–f_D–$C_{\rm sh}$ analyses respectively. The mean values for these sampled posterior distributions are centered around $\alpha \approx 0.21$, $\beta \approx 0.07$, with the exception of the 3D α–β analysis with its smaller mean α value of 0.16. The contours of these analyses are consistent (i.e., overlapping to some degree), and the posterior distributions from the α–β–BC–σ_D–f_D–$C_{\rm sh}$ analysis appear to be a superset of the smaller analyses.

Panels (b) and (c) of Figure 8 display the α–β joint posteriors for the "no λ PI" TTMs, respectively for the 2D model and the 3D model. See Section 4.4. In both cases, contours for the α–β analysis strongly follow the $\alpha = 2\beta$ line. The other analyses display steeper correlations and have contours distinct from the α–β analysis contours. It appears that the α–β analyses are too restricted, with the posterior constraints being driven to a different region of parameter space compared to the extended analyses of the same TTMs. This results in poor performance for these models, as discussed further in Section 5.2.

5.1.2. Extended Correlations

For the extended analyses (Section 4.2), there are additional joint-posterior distributions to examine; i.e., not just those for α and β. Figure 9 shows the joint-posterior distributions for some of these, specifically for the parameters β–f_D, $C_{\rm sh}$–f_D, $C_{\rm sh}$–α, and $C_{\rm sh}$–β. We omit discussion of other joint-posterior correlations.

The "cleanest" set of correlations occurs for $C_{\rm sh}$-α, being strong and positive for all models (Figure 9(c)). Intuitively, when the energy injection due to shear increases, the dissipation rate will increase, and, with vKH-style modeling, this can show up as an increase in the energy dissipation parameter α.

The two turbulence driving parameters, $C_{\rm sh}$ and f_D, show a negative correlation for the "standard" 2D TTM (Figure 9(b)), but for the 2D TTM with no $\dot{E}_{\rm PI}$ term in the λ equation (Section 4.4), $C_{\rm sh}$ is found to be almost independent of f_D. The negative correlation is an intriguing relation, as the shear driving term decays with radial distance ($\propto 1/r$), whereas $\dot{E}_{\rm PI}$ increases (nonlinearly) with distance; see Equation (8). The correlation may arise because, as far as determining $C_{\rm sh}$ and f_D is concerned, the two forms of driving compete to some degree, and this is apparent in Figure 9(b). For example, when the objective is for the TTM to match the observations, making $C_{\rm sh}$

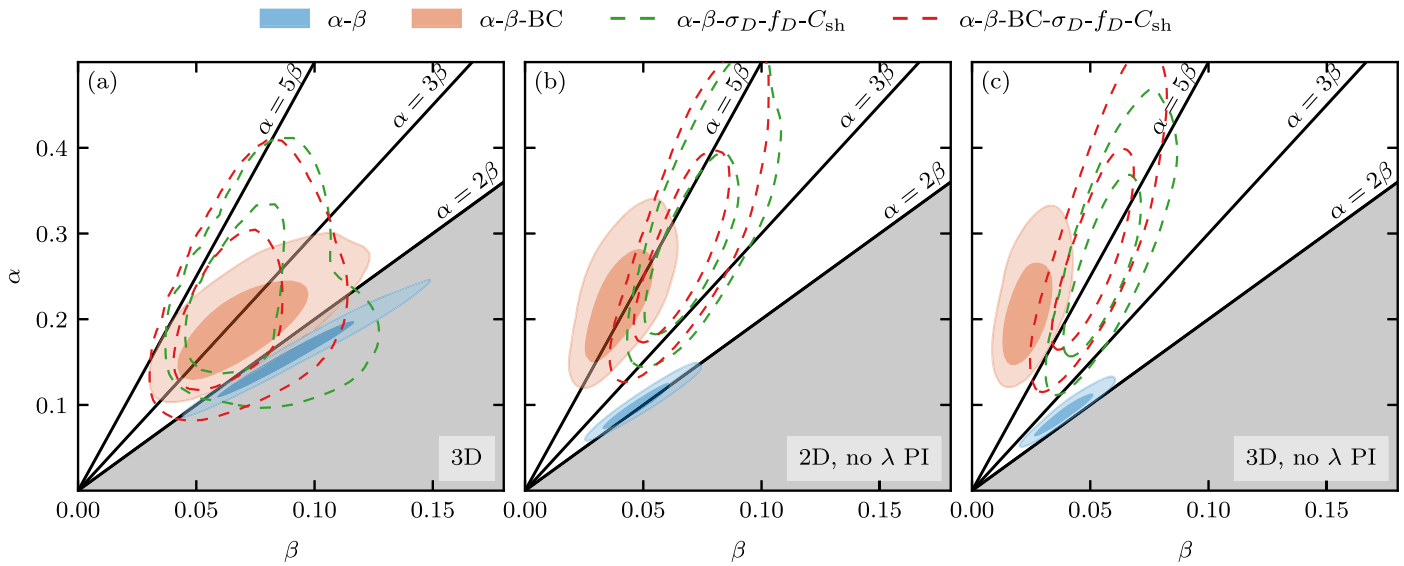

Figure 8. As for Figure 7(a) except for the (a) 3D TTM model, (b) 2D TTM model with no PI term in the λ equation, and (c) 3D TTM model with no PI term in the λ equation. Four analysis cases are shown in each panel: α–β (blue contours), α–β–BC (orange contours), α–β–σ_D–f_D–$C_{\rm sh}$ (green dashed), and α–β–BC–σ_D–f_D–$C_{\rm sh}$ (red dashed).

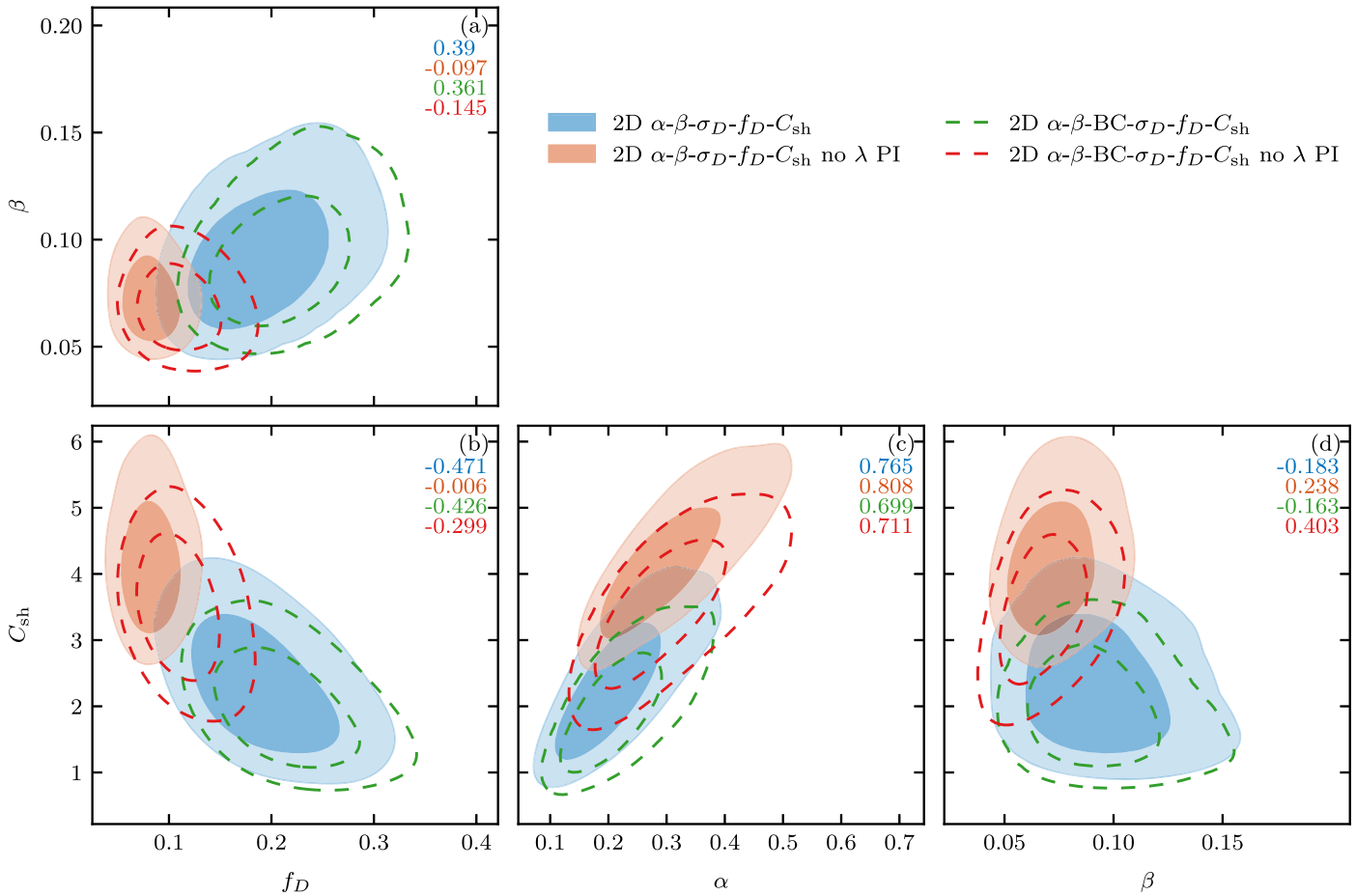

Figure 9. Joint-posterior distributions for the parameters α, β, f_D, and $C_{\rm sh}$ for four different 2D model analysis cases (see legend). The two analyses labeled with "no λ PI" refer to those discussed in Section 4.4. Numerical values in the top right corners of each panel are the Pearson correlation coefficients.

larger is associated with a reduced requirement for PI energy injection (i.e., f_D can be smaller). Another possibility is that the correlation is not really physical, but rather an artifact connected with limitations of the modeling, such as $C_{\rm sh}$ being constant at all distances, which conflicts with results from the split data set analysis of Section 4.3. Further investigation is required, but these results indicate that the TTMs require energy injection to best match the observations, as is well

known from previous studies (e.g., G. P. Zank et al. 1996; W. H. Matthaeus et al. 1999; J. D. Richardson & C. W. Smith 2003).

TTMs that lack the $\dot{E}_{\rm PI}$ term in the λ equation show no, or weak, correlations of f_D and β (Figure 9(a)). This is expected since there is then no direct coupling of the PI driving to the λ evolution; indirect effects, via Z, remain. However, these "no λ PI" TTMs show a positive correlation between $C_{\rm sh}$ and β (Figure 9(d)). Since $C_{\rm sh}$ is not present in the λ evolution equation (Equation (2)), this correlation must arise indirectly via couplings to the other equations. Conversely, for the "standard" TTMs, there is a weak positive correlation between β and f_D and little to no correlation between β and $C_{\rm sh}$.

Analyzing the correlations and/or degeneracies of the posterior distributions gives hints at the physics being modeled and can help critique constraints on the model parameters. Some of these relations between pairs of parameters are difficult to parse, in part due to the coupled nonlinear nature of the system of equations.

5.2. Model Selection

To compare models, we may use the Bayesian evidence values (Equation (12)) to calculate the *Bayes factor*, $\ln K = \ln \mathcal{Z}_{\rm model} - \ln \mathcal{Z}_{\rm fiducial}$. This factor is often used in Bayesian analysis to help determine whether or not a model is more strongly supported by the data relative to a fiducial model. We use the commonly accepted Jeffreys' scale (S. H. Jeffreys & S. H. Jeffreys 1998): $0.0 \leqslant |\ln K| < 1.0$ implies no favorability, $1.0 \leqslant |\ln K| < 3.0$ implies slight favorability, $3.0 \leqslant |\ln K| < 5.0$ is significant favorability, and $5.0 \leqslant |\ln K|$ is decisive favorability, with the phrases no/slight/significant/decisive favorability used as jargon. Since $\ln K = -\ln 1/K$, positive values imply reversed model favoring, i.e., we favor the comparison model over the fiducial. Comparisons between two nonfiducial models can be quantified by subtracting the two Bayes factors.

Table 5 lists the Bayes factors obtained when the fiducial model is the 2D α–β analysis. The lower section is for analyses run using the model without the PI term in the λ evolution equation (Section 4.4). Bluntly, the fiducial model is significantly too decisively favored relative to all the other analyses.

For the analyses where the TTM's λ equation does contain the $\dot{E}_{\rm PI}$ term (top section of Table 5), the fiducial 2D α–β analysis is decisively favored against the 3D α–β analysis. Similarly, the 2D α–β–σ_D–f_D–$C_{\rm sh}$ analysis is decisively favored against its 3D version. These outcomes accord with observational indications that MHD-scale solar wind fluctuations are predominantly quasi-2D in nature (e.g., J. W. Belcher & L. Davis 1971; W. H. Matthaeus et al. 1990; J. W. Bieber et al. 1996; C. W. Smith et al. 2006b), and with theoretical and numerical expectations regarding anisotropy relative to a large-scale magnetic field (e.g., J. V. Shebalin et al. 1983; V. Carbone & P. Veltri 1990; S. Oughton et al. 1994, 2015; W. H. Matthaeus et al. 1996a; P. Goldreich & S. Sridhar 1997; S. Oughton & W. H. Matthaeus 2020; A. A. Schekochihin 2022). The models with uncertainty in the BC conditions, α–β–BC, and α–β–BC–σ_D–f_D–$C_{\rm sh}$, have slight favorability to no favorability (respectively) for their 2D versions.

When we exclude the $\dot{E}_{\rm PI}$ term from the λ evolution equation (Section 4.4), the 2D α–β analysis is still decisively favored over the 3D. The 2D α–β–σ_D–f_D–$C_{\rm sh}$ analysis is only slightly favored over its 3D model. The two analyses with the BCs show no favorability to either the 2D or the 3D model.

By comparing the upper and lower sections of Table 5, we can assess whether including the PI driving term in the λ evolution equation is a useful modeling assumption to make. We see that the fiducial model is favored over any of the models that exclude PI driving from the λ equation. In fact, almost all combinations of the inclusion of the $\dot{E}_{\rm PI}$ term in the λ equation are decisively favored compared to the same analysis excluding this term. Furthermore, the α–β analysis of TTMs without an $\dot{E}_{\rm PI}$ term in the λ equation is decisively disfavored compared to any of the other analyses. When the PIs are not directly influencing λ, the best result is decisively the α–β–σ_D–f_D–$C_{\rm sh}$ analysis, with slight favorability to the 2D model.

Our discussion in this section has shown the power of Bayesian analysis in connection with TTMs, and we have seen that it can provide insights regarding model development. In particular, Bayesian analysis indicates that, of the models considered, the 2D TTM is a better fit than the 3D one, and that it is beneficial to include the PI driving term in the length scale equation. We also see a preference for the simpler analyses, that is, ones that constrain a smaller number of parameters. This is because the evidence is defined as the integral over the parameter space (Equation (12)). Bayesian models with more parameters available will require much lower χ^2 (Equation (11)), relative to the simpler models, to compensate for the increase caused by integrating over the larger region. Visually, it appears that most models produce similar results (compare Figures 1 and 4), indicating that the Bayesian modeling of additional parameters does not net a significant accuracy boost. That is, the data apparently lack sufficient information to constrain the extra parameters well.

6. Conclusions

We have shown that Bayesian analysis can be used to constrain values of adjustable parameters present in a class of energy-containing solar wind TTMs. The analysis also provides quantification regarding the consistency of a TTM with observational data. Additionally, we have shown how Bayesian evidence (in the form of readily computed Bayes factors) may be used to objectively compare distinct TTMs and thus select a preferred TTM.

Our solar wind data come from two sources: the PSP and Voyager 2 spacecraft missions. We have analyzed the compatibility of the solar wind data sets by performing the Bayesian analysis on the two data sets separately, and then together. The analysis with the combined data sets is able to place stronger, and consistent (with the separate data set analyses) constraints on the solar wind transport model parameters. We also analyzed how the TTM parameters might vary between conceptually distinct physical regions, such as inside and outside 5 au. The results match physical expectations that the inner-heliosphere data predominates for constraints on the initial conditions and $C_{\rm sh}$ parameter, while the outer-heliosphere data better constrain the strength of the PI driving, f_D. We find a slight discrepancy between the inner- and outer-heliosphere values for $C_{\rm sh}$, suggesting that this approach to modeling large-scale velocity shear (i.e., $C_{\rm sh} U Z^2/r$) has shortcomings. We note that other models for the shear driving exist (e.g., T. Wiengarten et al. 2015; G. P. Zank et al. 2017). In particular, G. P. Zank et al. (2017) propose a model with r^{-2}

dependence, and this different scaling may be able to better address the decrease in the $C_{\rm sh}$ parameter with radial distance associated with the present Bayesian analysis. Investigation of this is left for future work.

The joint-posterior distributions display behavior consistent with known behavior of the vKH parameters for homogeneous turbulence. We have also investigated the link between the vKH parameters with the turbulence driving coefficients. These relations imply extended forms of the homogeneous turbulence conservation property $Z^{2\beta/\alpha}\lambda = \text{const}$.

Using the Bayesian evidences, we decisively rule out the 3D isotropic turbulence assumption, in favor of fluctuations that are isotropic in 2D planes with respect to the large-scale magnetic field. This is consistent with observed and expected (anisotropic) dynamics in the solar wind. The model evidences also indicate that explicit inclusion of pickup ion effects in the correlation length equation—with the term obtained by assuming that $Z^{2\beta/\alpha}\lambda$ is locally conserved—is decisively favored over excluding this term.

The analysis discussed in Appendix B indicates that, for the considered TTMs, the fraction of cascaded turbulence energy that heats solar wind protons is $0.2 \lesssim \alpha_T \lesssim 1$ and that this depends nonlinearly on the α, f_D, and $C_{\rm sh}$ values. Given the small nominal estimates for f_D and $C_{\rm sh}$ (Table 1), we expect $0.6 \lesssim \alpha_T \lesssim 1$. Moreover, although we use $\alpha_T = 1$ in the main body of the paper, the considered TTMs are not very sensitive to the specific value of α_T used. Indeed, TTM solutions using α_T in this range have radial profiles that are visually very similar (see, e.g., Figures 4 and 11). We intend to investigate this more thoroughly in future work.

Consequently, based on the analysis of the particular TTMs and data sets employed herein, we recommend use of the 2D TTM with $\alpha = 0.16 \pm 0.03$, $\beta = 0.10 \pm 0.02$, the parameters stated in Table 1, and inclusion of PI effects in the lengthscale evolution equation. Naturally, these parameter values (as determined by the posterior distribution Equation (9)) depend on both the particular data sets analyzed, and the class of TTMs. Nonetheless, given the considerable scatter of much of the observational data, we anticipate that the values may be relatively robust for the solar wind conditions considered.

In closing, we note that the Bayesian analysis may be readily extended to more sophisticated solar wind models and their parameters. Such extensions might involve the six equation models of L. Adhikari et al. (2015, 2021), D. Shiota et al. (2017), and J. Kleimann et al. (2023), inclusion of a decelerating solar wind (C. Wang & J. Richardson 2003; P. A. Isenberg et al. 2010; H. A. Elliott et al. 2019), two-component models (S. Oughton et al. 2011; T. Wiengarten et al. 2016; G. P. Zank et al. 2017), and dynamic large-scale fields (A. V. Usmanov et al. 2011; T. Wiengarten et al. 2015; A. V. Usmanov et al. 2016; J. Kleimann et al. 2023). The analysis may also be employed with space weather models and might lead to improved predictions of, for example, solar flare and coronal mass ejection interactions with Earth.

7. Author Contributions

M.A.B. contributed conceptualization, analysis, interpretation, discussions, manuscript preparation, and writing. S.O. contributed transport model expertise, interpretation, discussions, significant manuscript writing, and review. T.N.P. contributed interpretation, discussions, manuscript writing, and review. Y.C.P. contributed Bayesian analysis expertise, interpretation, discussions, manuscript review, and editing.

Acknowledgments

Research supported by the Marsden Fund Council from NZ Government funding, managed by Royal Society Te Apārangi (E4200). We are grateful to Dr. C. W. Smith for kindly providing access to the proton temperature Voyager 2 solar wind observational data set from their paper (C. W. Smith et al. 2006a). We also thank Dr. L. Adhikari for providing the derived turbulence energy and correlation length, and proton and electron temperature data from his papers (L. Adhikari et al. 2015, 2021). These data were derived from NASA Parker Solar Probe, Voyager 2, and Ulysses magnetometer and plasma data sets. We thank the anonymous referee for helpful suggestions that have improved the presentation of this paper.

Software: Python: multinest, pymultinest, fgivenx, getdist, sympy, matplotlib, astropy, numpy, scipy, pandas.

Appendix A
Updated Breech et al. (2008) Model

B. Breech et al. (2008) presented a four-equation model for the time-steady radial transport of solar wind fluctuations in prescribed background solar wind fields:

$$U\frac{dZ^2}{dr} = -\frac{UZ^2}{r}[1 + \sigma_D M_Z - C_{\rm sh}] + \dot{E}_{\rm PI} - \alpha f^+(\sigma_c)\frac{Z^3}{\lambda}, \tag{A1}$$

$$U\frac{d\lambda}{dr} = \beta f^+(\sigma_c)Z - \frac{\beta}{\alpha}\frac{\lambda}{Z^2}\dot{E}_{\rm PI}, \tag{A2}$$

$$U\frac{d\sigma_c}{dr} = \alpha f'(\sigma_c)\frac{Z}{\lambda} - \left[\frac{U}{r}(C_{\rm sh} - \sigma_D M_Z) + \frac{\dot{E}_{\rm PI}}{Z^2}\right]\sigma_c, \tag{A3}$$

$$U\frac{dT}{dr} = -\frac{4}{3}\frac{TU}{r} + \frac{\alpha}{3}\frac{m_p}{k_{\rm B}}f^+(\sigma_c)\frac{Z^3}{\lambda}, \tag{A4}$$

where we employ the same notation used in the body of the present paper.

This is actually two models—one for fluctuations that are (3D) isotropic and one for fluctuations that are 2D with respect to the large-scale magnetic field (and isotropic in the 2D planes). The distinction between the models enters via the (energy) mixing operator

$$M_Z = \begin{cases} \frac{1}{3}, & \text{3D} \\ \cos^2\psi, & \text{2D}. \end{cases} \tag{A5}$$

Unfortunately a mistake was made during the derivation of the lengthscale equation (Equation (A2)). Specifically, when integrating their Equation (17), over the lag ζ, the $\zeta = 0$ forms of $R_{ij}^{D,s}(\zeta)$ were used rather than the full correlation functions (see Appendix B in J. Kleimann et al. 2023). Rectifying this yields the updated equation for $L(r) = \int_0^\infty R_{jj}(r, \zeta)\, d\zeta$ and thence the updated equation for $\lambda = L/Z^2$:

$$U\frac{d\lambda}{dr} = \frac{\lambda\sigma_D M_\lambda U}{r} + \beta f^+(\sigma_c)Z - \frac{\beta}{\alpha}\frac{\lambda}{Z^2}\dot{E}_{\rm PI}\,, \tag{A6}$$

which is Equation (2) in Section 2. This contains a new term involving the λ mixing operators

$$M_\lambda = \begin{cases} \frac{1}{3}, & \text{3D} \\ \sin^2\psi, & \text{2D} \end{cases}, \tag{A7}$$

where the closure $\lambda_D = \lambda$ has been used in $L_D = \lambda_D D$.

Note that for the model evolving 2D fluctuations there is a subtlety to the interpretation of λ. To make contact with solar wind observations, correlation functions are calculated using *radial* lags—rather than lags in the 2D plane. Consequently, if λ^{2D} is the in-plane correlation length, the λ appearing in the model equations above (obtained after integrating the correlation functions over radial lag) is actually $\lambda^{2D}/\sin\psi$, which is larger than the "true" value.

Appendix B
Turbulence Dissipation and Proton and Electron Heating

In the solar wind, not all of the cascaded turbulence energy heats solar wind protons, with some of it instead heating electrons (see, e.g., B. Breech et al. 2009; S. R. Cranmer et al. 2009; G. G. Howes 2011; L. Adhikari et al. 2021; R. Bandyopadhyay et al. 2023). The details governing this partitioning are not well understood and thus represent another interesting candidate to apply Bayesian analysis to.

To investigate this, we modify the turbulent heating term in the (proton) temperature (Equation (4)) to include an additional parameter $\alpha_T \in [0, 1]$,

$$U\frac{dT}{dr} = -\frac{4}{3}\frac{TU}{r} + \alpha_T \frac{\alpha}{3}\frac{m_p}{k_B} f^+(\sigma_c)\frac{Z^3}{\lambda}. \tag{B8}$$

This parameter describes the fraction of turbulence energy that is injected into the proton temperature (with the rest assumed to go toward electron scales). The Bayesian analyses in Section 4 can be thought of as having a δ-function prior that mandates $\alpha_T = 1$. We perform two 2D TTM Bayesian analyses: α–β–α_T, and α–β–BC–σ_D–f_D–C_{sh}–α_T using the corresponding priors stated in Tables 2 and 4, and using a uniform distribution on [0.1, 1] as the prior for α_T.

Figure 10 displays some of the joint-posterior distributions for the 2D α–β–α_T and α–β–BC–σ_D–f_D–C_{sh}–α_T analyses. Note the "banana" shape of the α–β–BC–σ_D–f_D–C_{sh}–α_T posterior distributions. Such shapes can be problematic to interpret and indicate that the associated 1D posteriors can be misleading. For example, the 1D posterior distribution for α_T (Figure 10(g)) seems strongly peaked at $\approx$0.4. However, the 95% confidence intervals for the joint-posterior distributions for α_T indicate a (much wider) range between 0.2 and 0.9. We also see that the 2D α–β–α_T analysis is strongly pushed up against the upper boundary of the α_T prior (with $\alpha_T > 1$ being unphysical behavior) and gives mean values of $\alpha_T \approx 0.93$ and an α and β that are equal to those from the 2D α–β analysis. The joint posteriors thus indicate that the choice of the δ-function prior for $\alpha_T = 1$ effectively restricts the posterior distributions of the other parameters (α, f_D, and C_{sh}) to the smaller values obtained in Sections 4 and 5.

Solutions to the TTM (with α_T) are shown in Figure 11. Comparing this with Figure 4, one sees that the introduction of α_T produces only small differences. This similarity suggests that the TTMs contain more parameters than can be constrained effectively by the available observational data (see Section 5.2).

Log-evidences for the two α_T analyses are given in Table 6 and indicate only slight favorability for the 2D TTM α–β analysis over the 2D TTM α–β–α_T analysis. There is no favorability for the 2D α–β–BC–σ_D–f_D–C_{sh} analysis over the 2D α–β–BC–σ_D–f_D–C_{sh}–α_T analysis. In other words, adding the α_T parameter has not yielded any better performance of the TTM (this is supported by the similar solutions in Figures 4–11). The simplest 2D TTM α–β analysis remains the favored model, likely for similar reasons to those discussed in Section 5.2.

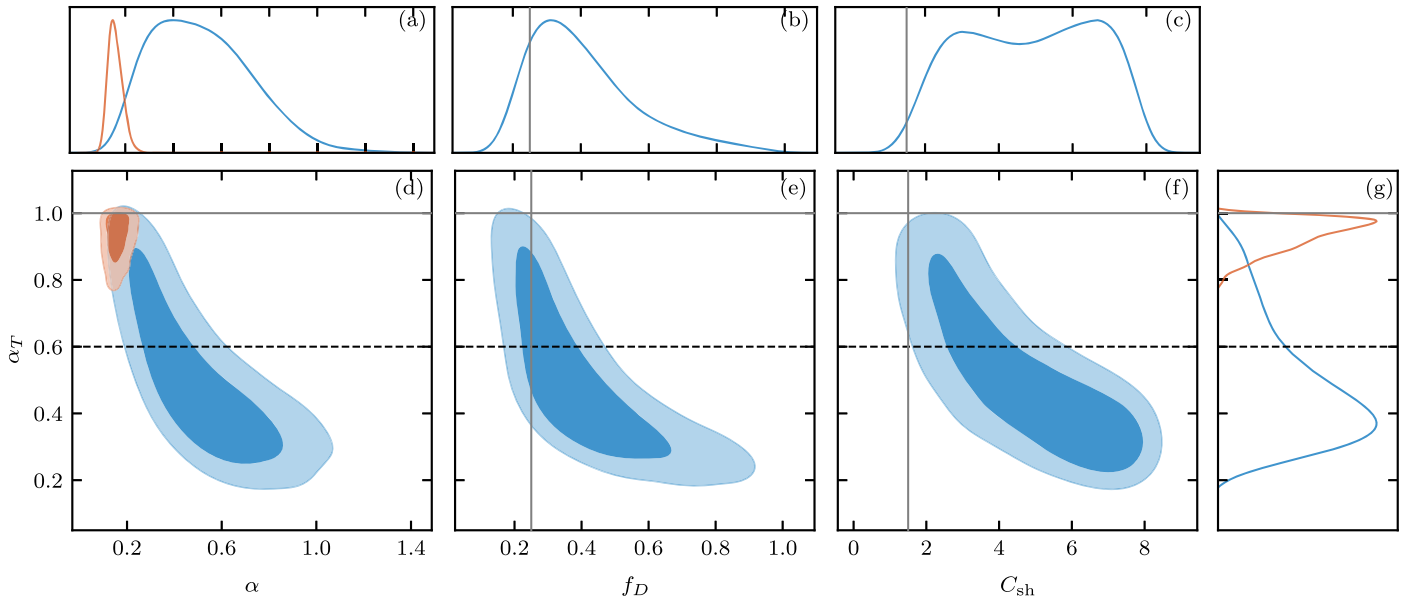

Figure 10. 2D α–β–α_T (orange) and 2D α–β–BC–σ_D–f_D–C_{sh}–α_T (blue) joint-posterior distributions for the parameters α_T with α, f_D, and C_{sh} (panels (d), (e), and (f), respectively) as well as 1D posterior distributions for α, f_D, C_{sh}, and α_T (panels (a), (b), (c), and (g), respectively). The solid gray vertical and horizontal lines are the nominal estimates, i.e., the assumed values for the analyses that do not constrain these variables; see Table 1. The horizontal black dashed line at $\alpha_T = 0.6$ is as reported on in B. Breech et al. (2009) and S. R. Cranmer et al. (2009).

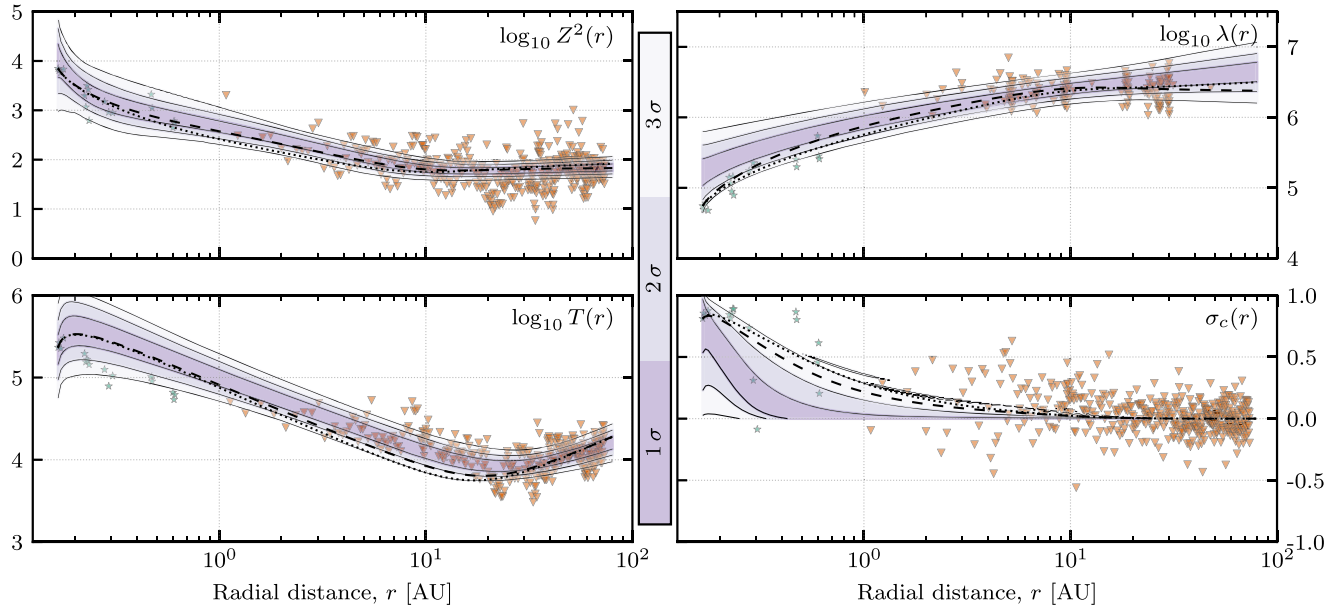

Figure 11. Solutions for the 2D α–β–BC–σ_D–f_D–$C_{\rm sh}$–α_T analysis. The contours represent the confidence intervals of the means in the solutions obtained by the sampled posterior distributions. Green stars indicate PSP data, and orange triangles Voyager 2 data. The 2D and 3D TTM posterior sampled means of the α–β analysis (i.e.,with $\alpha_T = 1$) are plotted with dashed and dotted black lines respectively. Units are as in Table 3.

Table 6
Bayes Factors, $\ln K = \ln \mathcal{Z}_{\rm model} - \ln \mathcal{Z}_{\rm fiducial}$, for the 2D TTMs That Use Equation (B8)

Analysis	2D
α–β–α_T	−1.87
α–β–BC–σ_D–f_D–$C_{\rm sh}$–α_T	−10.28

Note. To obtain $\mathcal{Z}_{\rm fiducial}$, we use the 2D α–β analysis (see Table 5).

Considering the shape of the α–β–BC–σ_D–f_D–$C_{\rm sh}$–α_T joint-posterior distributions in Figure 10, with small estimates for f_D and $C_{\rm sh}$, we see similar preference in the Bayesian analysis for values $0.6 \lesssim \alpha_T \lesssim 1$. Imposing the nominal estimates for f_D and $C_{\rm sh}$ (Table 1) leads to a reduced range of $0.8 \lesssim \alpha_T \lesssim 1$.

Given the observational results that $\alpha_T \sim 0.6$ (B. Breech et al. 2009; S. R. Cranmer et al. 2009; R. Bandyopadhyay et al. 2023), this set of features—the range of likely α_T values, the log-evidence values in Table 6, and the similarity of the solutions shown in Figures 4 and 11—suggests that the TTMs considered herein may have shortcomings, as far as matching observational data is concerned. An alternative possibility is that more observational data are required to adequately constrain the TTM parameters.

Appendix C
Bayesian Methodologies

Evaluation of the evidence $\mathcal{Z}(\mathcal{D})$ (Equation (12)) is usually ignored for parameter estimation since it is independent of the parameters Θ. With this approach, parameter estimation inferences are typically obtained by taking samples from the unnormalized posterior, for example using Markov Chain Monte Carlo methods. However, for comparison of models, $\mathcal{Z}(\mathcal{D})$ is required, and evaluation of this multidimensional integral can be numerically challenging.

To calculate $\mathcal{Z}(\mathcal{D})$, we use *nested sampling* (see, G. Ashton et al. 2022, for a review on nested sampling, and its use with physical applications), which reformulates $\mathcal{Z}(\mathcal{D})$ into a 1D integral over contour regions of the likelihood (J. Skilling 2004; F. Feroz & M. P. Hobson 2008; F. Feroz et al. 2009):

$$\mathcal{Z}(\mathcal{D}) = \int_0^1 \mathcal{L}(X) dX, \tag{C9}$$

where

$$X(\lambda) = \int_{\mathcal{L}(\Theta)>\lambda} \pi(\Theta)\, d^D\Theta. \tag{C10}$$

This simplifies the calculation, and provides an efficient method for providing parameter constraints and model evidences. By *independently* selecting parameter values Θ, we can evaluate the corresponding likelihood, that is, how likely it is that these chosen parameters are able to reproduce the observed data. Recursively sampling new parameter values allows iterative estimation of their (posterior) distributions. These may be employed to constrain parameters present in solar wind transport models, and the evidence $\mathcal{Z}(\mathcal{D})$ used to compare different models.

In our analysis, we use the python interface `pymultinest` (J. Buchner 2016) to `multinest` (F. Feroz et al. 2009), where the latter implements a multimodal nested-sampling algorithm. This Bayesian inference tool calculates the evidence and produces posterior samples from distributions that may be multimodal, or exhibit complex degeneracies in high dimensional data. Using `pymultinest`, we can obtain constraints on the parameters by repeatedly solving the model with different parameter values. Approximate analysis runtimes, and the number of likelihood evaluations (roughly the number of times we need to solve the system of differential equations) are provided in Table 7. By default, `multinest` automatically runs until the parameter sampling has converged; this is essential to obtain accurate integration over likelihood contour levels. We use the number of live points as 100 times the number of parameters we are sampling, with a default sampling efficiency of 0.8. An example of convergence of parameter sampling is shown in Figure 12, where the α and β parameters are plotted as a function of their sampling number (i.e., simply plotting the chains provided by

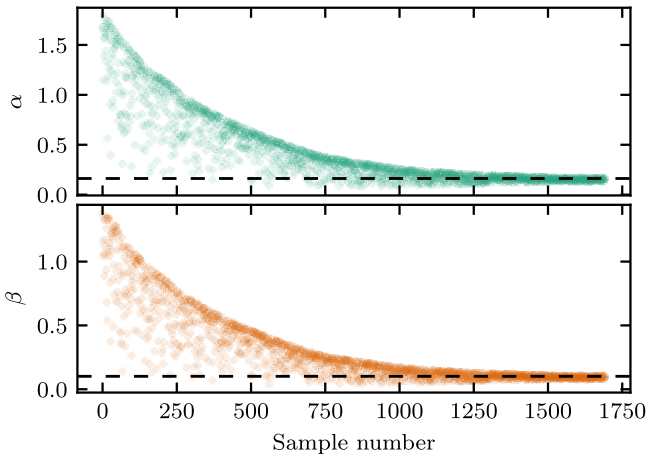

Figure 12. The samples of the 2D α–β analysis, showcasing the convergence of the α–β parameters toward the mean sampled posterior values (horizontal, black, dashed line).

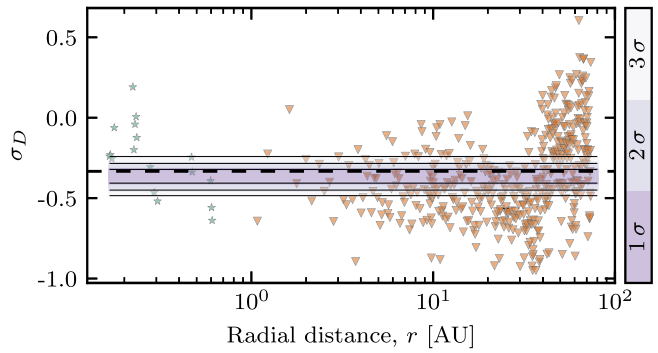

Figure 13. Same format as Figure 4. Solutions for σ_D from the 2D α–β–BC–σ_D–f_D–$C_{\rm sh}$ analysis. Green stars show the PSP data, and orange triangles the Voyager 2 data. The horizontal black dashed line shows the value $\sigma_D \approx -1/3$ that we employ in analyses that do not constrain σ_D.

Table 7
Execution Times and Number of Likelihood Evaluations for Bayesian Analysis Using `multinest` on a Desktop Computer with 32 GB RAM, and an 8 Core, 4 GHz CPU

Model	Time (minutes)	Num. Evaluations
α–β	2	3000
α–β–BC	10	25,000
α–β–σ_D–f_D–$C_{\rm sh}$	10	25,000
α–β–BC–σ_D–f_D–$C_{\rm sh}$	40	90,000

`multinest`), which corresponds to the time of sampling. In the case of both parameters, the whole prior distribution is sampled to start with, then the chains converge toward the mean sampled posterior value. The output of `multinest` can provide the weighted mean, maximum likelihood, or maximum a posteriori estimate. This output is used to determine a "best" solution for the constrained parameters.

To examine the sampled posterior distributions provided by `multinest` and generate the joint-posterior and 1D posterior distributions and confidence interval plots (such as Figure 13), we make use of the public domain routines `getdist`[10] (A. Lewis 2019) and `fgivenx`[11] (W. Handley 2018).

[10] https://github.com/cmbant/getdist
[11] https://github.com/handley-lab/fgivenx

ORCID iDs

Mark A. Bishop https://orcid.org/0009-0002-8645-5139
Sean Oughton https://orcid.org/0000-0002-2814-7288
Tulasi N. Parashar https://orcid.org/0000-0003-0602-8381
Yvette C. Perrott https://orcid.org/0000-0002-6255-8240

References

Abbott, T. M. C., Allam, S., Andersen, P., et al. 2019, ApJL, 872, L30
Adhikari, L., Zank, G. P., Bruno, R., et al. 2015, ApJ, 805, 63
Adhikari, L., Zank, G. P., Hunana, P., et al. 2017a, ApJ, 841, 85
Adhikari, L., Zank, G. P., Telloni, D., et al. 2017b, ApJ, 851, 117
Adhikari, L., Zank, G. P., & Zhao, L. 2021, Fluid, 6, 368
Adhikari, L., Zank, G. P., Wang, B., et al. 2023, ApJ, 953, 44
Ashton, G., Bernstein, N., Buchner, J., et al. 2022, NRvMP, 2, 39
Bandyopadhyay, R., Matthaeus, W. H., Oughton, S., & Wan, M. 2019, JFM, 876, 5
Bandyopadhyay, R., Meyer, C. M., Matthaeus, W. H., et al. 2023, ApJL, 955, L28
Bandyopadhyay, R., Oughton, S., Wan, M., et al. 2018, PhRvX, 8, 041052
Barbary, K. 2021, nestle: Nested sampling algorithms for evaluating Bayesian evidence, Astrophysics Source Code Library, ascl:2103.022
Belcher, J. W., & Davis, L. 1971, JGR, 76, 3534
Bieber, J. W., Wanner, W., & Matthaeus, W. H. 1996, JGR, 101, 2511
Breech, B., Matthaeus, W. H., Cranmer, S. R., Kasper, J. C., & Oughton, S. 2009, JGR, 114, A09103
Breech, B., Matthaeus, W. H., Minnie, J., et al. 2008, JGR, 113, A08105
Breech, B., Matthaeus, W. H., Minnie, J., et al. 2005, GeoRL, 32, L06103
Brewer, B. J., Pártay, L. B., & Csányi, G. 2010, DNEST: Diffusive Nested Sampling, Astrophysics Source Code Library, ascl:1010.029
Bruno, R., & Carbone, V. 2013, LRSP, 10, 2
Buchner, J. 2016, PyMultiNest: Python interface for MultiNest, Astrophysics Source Code Library, ascl:1606.005
Buchner, J. 2021, JOSS, 6, 3001
Burlaga, L. F. 1974, JGR, 79, 3717
Carbone, V., & Veltri, P. 1990, GApFD, 52, 153
Corsaro, E., & De Ridder, J. 2014, A&A, 571, A71
Cranmer, S. R., Matthaeus, W. H., Breech, B. A., & Kasper, J. C. 2009, ApJ, 702, 1604
Cuesta, M. E., Chhiber, R., Roy, S., et al. 2022a, ApJL, 932, L11
Cuesta, M. E., Parashar, T. N., Chhiber, R., & Matthaeus, W. H. 2022b, ApJS, 259, 23
Dryden, H. L. 1943, QApMa, 1, 7
Elliott, H. A., McComas, D. J., Zirnstein, E. J., et al. 2019, ApJ, 885, 156
Ellison, A. M. 2004, EcolL, 7, 509
Engelbrecht, N. E., Effenberger, F., Florinski, V., et al. 2022, SSRv, 218, 33
Feroz, F., & Hobson, M. P. 2008, MNRAS, 384, 449
Feroz, F., Hobson, M. P., & Bridges, M. 2009, MNRAS, 398, 1601
Fraternale, F., Adhikari, L., Fichtner, H., et al. 2022, SSRv, 218, 50
Goldreich, P., & Sridhar, S. 1997, ApJ, 485, 680
Handley, W. 2018, JOSS, 3, 849
Handley, W. J., Hobson, M. P., & Lasenby, A. N. 2015, MNRAS, 453, 4384
Hellinger, P., Trávníček, P. M., Štverák, V., Matteini, L., & Velli, M. 2013, JGR, 118, 1351
Hojjati, A., Pogosian, L., & Zhao, G.-B. 2011, JCAP, 2011, 005
Hossain, M., Gray, P. C., Pontius, D. H., Matthaeus, W. H., & Oughton, S. 1995, PhFl, 7, 2886
Howes, G. G. 2011, ApJ, 738, 40
Huang, Y., Shao, C., Wu, B., Beck, J. L., & Li, H. 2019, Advances in Structural Engineering, 22, 1329
Isenberg, P. A. 2005, ApJ, 623, 502
Isenberg, P. A., Smith, C. W., & Matthaeus, W. H. 2003, ApJ, 592, 564
Isenberg, P. A., Smith, C. W., Matthaeus, W. H., & Richardson, J. D. 2010, ApJ, 719, 716
Javid, K., Perrott, Y. C., Rumsey, C., & Saunders, R. D. E. 2019, MNRAS, 489, 3135
Jeffreys, S. H., & Jeffreys, S. H. 1998, The Theory of Probability (3rd ed.; Oxford: Oxford Univ. Press),
Jungman, G., Kamionkowski, M., Kosowsky, A., & Spergel, D. N. 1996, PhRvD, 54, 1332
Kester, D., & Mueller, M. 2021, BayesicFitting, aA PYTHON Toolbox for Bayesian Fitting and Evidence Calculation, Astrophysics Source Code Library, ascl:2112.020
Kleimann, J., Oughton, S., Fichtner, H., & Scherer, K. 2023, ApJ, 953, 133

Kolmogorov, A. N. 1941, CR, 31, 538
Lee, M., & Ip, W.-H. 1987, JGR, 92, 11041
Lewis, A. 2019, GetDist: Monte Carlo sample analyzer, Astrophysics Source Code Library, ascl:1910.018
Linkmann, M., Berera, A., & Goldstraw, E. E. 2017, PhRvE, 95, 013102
Matthaeus, W. H., Ghosh, S., Oughton, S., & Roberts, D. A. 1996a, JGR, 101, 7619
Matthaeus, W. H., Goldstein, M. L., & Roberts, D. A. 1990, JGR, 95, 673
Matthaeus, W. H., Oughton, S., Pontius, D., & Zhou, Y. 1994, JGR, 99, 267
Matthaeus, W. H., Zank, G. P., & Oughton, S. 1996b, JPlPh, 56, 659
Matthaeus, W. H., Zank, G. P., Smith, C. W., & Oughton, S. 1999, PhRvL, 82, 3444
McComas, D., Rankin, J., Schwadron, N., & Swaczyna, P. 2019, ApJ, 884, 145
Neugebauer, M., Goldstein, B. E., McComas, D. J., Suess, S. T., & Balogh, A. 1995, JGR, 100, 389
Oughton, S., & Engelbrecht, N. E. 2021, NewA, 83, 101507
Oughton, S., & Matthaeus, W. H. 2020, ApJ, 897, 37
Oughton, S., Matthaeus, W. H., Smith, C. W., Breech, B., & Isenberg, P. A. 2011, JGR, 116, A08105
Oughton, S., Matthaeus, W. H., Wan, M., & Osman, K. T. 2015, RSPTA, 373, 20140152
Oughton, S., Priest, E. R., & Matthaeus, W. H. 1994, JFM, 280, 95
Parashar, T. N., Cuesta, M., & Matthaeus, W. H. 2019, ApJL, 884, L57
Parker, E. N. 1958, ApJ, 128, 664
Parker, E. N. 1965, SSRv, 4, 666
Parkinson, D., & Liddle, A. R. 2013, SADM, 9, 3
Parkinson, D., Mukherjee, P., & Liddle, A. 2011, CosmoNest: Cosmological Nested Sampling, Astrophysics Source Code Library, ascl:1110.019
Pei, C., Bieber, J. W., Breech, B., et al. 2010, JGR, 115, A03103
Perlmutter, S., Pennypacker, C. R., Goldhaber, G., et al. 1995, ApJL, 440, L41
Perri, S., & Balogh, A. 2010, GeoRL, 37, L17102
Perrott, Y. C., Javid, K., Carvalho, P., et al. 2019, MNRAS, 486, 2116
Petzold, L. 1983, SIAM Journal on Scientific and Statistical Computing, 4, 136
Planck Collaboration, Aghanim, N., Akrami, Y., et al. 2020, A&A, 641, A6
Pogorelov, N. V., Arge, C. N., Caplan, R. M., et al. 2024, JPhCS, 2742, 012013
Richardson, J. D., & Smith, C. W. 2003, GeoRL, 30, 1206
Saffman, P. G. 1967, PhFl, 10, 1349
Schekochihin, A. A. 2022, JPlPh, 88, 155880501
Schwenn, R. 2006, LRSP, 3, 2
Sharma, S. 2017, ARA&A, 55, 213
Shebalin, J. V., Matthaeus, W. H., & Montgomery, D. 1983, JPlPh, 29, 525
Shiota, D., Zank, G. P., Adhikari, L., et al. 2017, ApJ, 837, 75
Skilling, J. 2004, in AIP Conf. Ser. 735, Bayesian Inference and Maximum Entropy Methods in Science and Engineering: 24th Int. Workshop on Bayesian Inference and Maximum Entropy Methods in Science and Engineering, ed. R. Fischer, R. Preuss, & U. V. Toussaint (Melville, NY: AIP), 395
Smith, C. W., Isenberg, P. A., Matthaeus, W. H., & Richardson, J. D. 2006a, ApJ, 638, 508
Smith, C. W., Matthaeus, W. H., Zank, G. P., et al. 2001, JGR, 106, 8253
Smith, C. W., & Vasquez, B. J. 2024, FrASS, 11, 1371058
Smith, C. W., Vasquez, B. J., & Hamilton, K. 2006b, JGR, 111, A09111
Smith, E. J., & Wolfe, J. H. 1976, GeoRL, 3, 137
Sokół, J. M., Kucharek, H., Baliukin, I. I., et al. 2022, SSRv, 218, 18
Speagle, J. S. 2020, MNRAS, 493, 3132
Sreenivasan, K. R. 1998, PhFl, 10, 528
Trotta, R. 2008, ConPh, 49, 71
Tu, C. 1987, SoPh, 109, 149
Tu, C.-Y., & Marsch, E. 1995, SSRv, 73, 1
Tu, C.-Y., Pu, Z.-Y., & Wei, F.-S. 1984, JGR, 89, 9695
Usmanov, A. V., Goldstein, M. L., & Matthaeus, W. H. 2014, ApJ, 788, 43
Usmanov, A. V., Goldstein, M. L., & Matthaeus, W. H. 2016, ApJ, 820, 17
Usmanov, A. V., Matthaeus, W. H., Breech, B. A., & Goldstein, M. L. 2011, ApJ, 727, 84
Usmanov, A. V., Matthaeus, W. H., Goldstein, M. L., & Chhiber, R. 2018, ApJ, 865, 25
van de Schoot, R., Depaoli, S., King, R., et al. 2021, Nat. Rev. Methods Primers, 1, 1
van der Holst, B., Sokolov, I. V., Meng, X., et al. 2014, ApJ, 782, 81
Velli, M., Grappin, R., & Mangeney, A. 1989, PhRvL, 63, 1807
von Toussaint, U. 2011, RvMP, 83, 943
Wan, M., Oughton, S., Servidio, S., & Matthaeus, W. H. 2012, JFM, 697, 296
Wang, C., & Richardson, J. 2003, JGRA, 108, 1058
Wiengarten, T., Fichtner, H., Kleimann, J., & Kissmann, R. 2015, ApJ, 805, 155
Wiengarten, T., Oughton, S., Engelbrecht, N. E., et al. 2016, ApJ, 833, 17
Williams, L. L., & Zank, G. P. 1994, JGR, 99, 229
Wrench, D., Parashar, T. N., Oughton, S., de Lange, K., & Frean, M. 2024, ApJ, 961, 182
Yokoi, N., Rubinstein, R., Hamba, F., & Yoshizawa, A. 2008, JTurb, 9, N37
Zank, G. P., Adhikari, L., Hunana, P., et al. 2017, ApJ, 835, 147
Zank, G. P., Adhikari, L., Zhao, L.-L., et al. 2018, ApJ, 869, 23
Zank, G. P., Dosch, A., Hunana, P., et al. 2012, ApJ, 745, 35
Zank, G. P., Matthaeus, W. H., & Smith, C. W. 1996, JGR, 101, 17093
Zhou, Y., & Matthaeus, W. H. 1990, JGR, 95, 10 291
Zirnstein, E. J., Möbius, E., Zhang, M., et al. 2022, SSRv, 218, 28